

Pattern formation in 2-frequency forced parametric waves

H. Arbell and J. Fineberg

The Racah Institute of Physics, The Hebrew University of Jerusalem, Jerusalem 91904, Israel

We present an experimental investigation of superlattice patterns generated on the surface of a fluid via parametric forcing with 2 commensurate frequencies. The spatio-temporal behavior of 4 qualitatively different types of superlattice patterns is described in detail. These states are generated via a number of different 3-wave resonant interactions. They occur either as symmetry-breaking bifurcations of hexagonal patterns composed of a single unstable mode or via nonlinear interactions between the two primary unstable modes generated by the two forcing frequencies. A coherent picture of these states together with the phase space in which they appear is presented. In addition, we describe a number of new superlattice states generated by 4-wave interactions that arise when symmetry constraints rule out 3-wave resonances.

PACS numbers: 47.54.+r, 47.35.+i, 47.20Gv

I. BACKGROUND

Patterns are ubiquitous in the world around us. The word “pattern” describes an order, regularity, or a simple mathematical description, which can be found either in a natural or man-made system. Patterns often result from self-interactions of driven nonlinear systems. Naturally, the first patterns to be scientifically analyzed were the simplest ones, which can be described by few mathematical variables. However, in recent years we have learned to recognize and categorize patterns in systems that were assumed to be formless, devoid of any order. Perhaps the most obvious characteristics of these systems are the multiple length and time scales that can be present simultaneously. One of the most important mechanisms to explain such phenomena is the nonlinear resonant interaction between the different modes that are excited in these systems. In these interactions two or more waves can interact to form “new” waves. These waves have a wavelength and frequency which is the sum or difference of the basic waves. The system’s energy can then be transferred between these modes or dissipated at different scales. The purpose of the work described in this paper was to explore this paradigm in the experimental study of a simple controlled system: the parametric excitation of waves on the surface of a fluid (the Faraday system).

The general form of the external acceleration applied to the system is given by:

$$g(t) = A[\cos(\chi) \cos(m\omega_0 t) + \sin(\chi) \cos(n\omega_0 t + \phi)] \quad (1)$$

This spatially uniform vertical excitation preserves the system’s spatial symmetries, while modifying its temporal ones.

As first noted by Faraday, sinusoidal acceleration (in the direction of gravity) of a fluid layer with angular frequency ω induces a pattern, having a wavenumber $k(\omega)$, on the fluid surface. Whereas waves excited by a single-frequency have been studied extensively over the last 4

decades, the response of the system for multi-frequency excitations has only recently begun to be investigated. Single-frequency driving can produce patterns of different symmetries. Patterns consisting of rolls, squares, hexagons and 8,10,12-fold quasi-patterns have been experimentally observed in [1–4]. The secondary instabilities of these different patterns involve complicated states that display either spatiotemporal chaos [5–8,3,9], transverse amplitude modulations [10] or various defects [3,10] that break the patterns’ initial global symmetry. The use of multiple-frequency driving enables us to study the interactions of different excited modes in a controlled way, as each excitation frequency can linearly excite a well-defined wavenumber. In this way, we hope to be able to slowly unfold the system’s underlying behavior and, thereby unravel the fundamental mechanisms that describe the waves’ interactions.

The purpose of this paper is to provide a coherent overview of the wide variety of nonlinear states that result from 2-frequency forcing. We will provide detailed descriptions of the spatial and temporal behavior of these states. In doing so, we will provide a characterization of these nonlinear states - depicting both the resonant mechanisms and symmetry constraints giving rise to their formation.

This paper is organized in the following fashion. In section I we will briefly describe the theoretical and experimental work that has, to date, been performed in this system. The experimental apparatus and measurement techniques used in our measurements will then be described in section II. We will then present, in section III, an overview of the phase diagram together with a brief description of the different types of superlattice states observed. Each type of superlattice, together with the mechanisms that form it, will then be described in detail in the subsequent sections. A codimension two point, at χ_c , exists in this system where both externally driven modes simultaneously become linearly unstable. Subharmonic Superlattice States (SSS), which bifurcate from an

initial hexagonal state far from χ_c , will be described in section IV. We will then progress to the region of phase space in the vicinity of χ_c . Three different types of superlattice patterns will be described in sections V, VI, and VII. All of the above superlattice patterns result from different types of 3-wave resonant interactions. We will conclude with section VIII in which a number of superlattice states generated by 4-wave resonant interactions are described. We will show that these states can occur when 3-wave interactions are forbidden.

A. Notation

The notation conventions used throughout this paper are as follows. The driving function is specified in Eq. (1). To avoid confusion, we will always specify the driving frequency ratio used in Eq. (1) by the ratio m/n where m and n are the two co-prime integers that describe the two frequencies $\omega_1 = m\omega_0$ and $\omega_2 = n\omega_0$. We will always assume that $n > m$. In our notation, k_1 and k_2 refer to the wavenumbers excited, respectively, by the driving frequencies ω_1 and ω_2 . The angle χ in Eq. (1) describes the relative mixing between the two modes and the angle ϕ describes their phase difference, where the relevant range is $0 < \phi < 2\pi m/n$. $\cos(\chi)$ and $\sin(\chi)$ are sometimes [11,12] replaced by the mixing coefficients r and $1 - r$.

In the following sections we will frequently characterize eigenmodes by their temporal parity. Since the parity of m and n is important we will use the notation odd/even (even/odd) to describe the classes of driving where m (n) is odd and n (m) is even. Odd/odd describes driving where both m and n are odd. A state whose temporal response has a fundamental frequency of $\omega_0/2$ will be denoted as a “subharmonic” state, whereas a “harmonic” state is one with a fundamental frequency of ω_0 .

We shall use the following units. The total amplitude A , appearing in Eq. (1), is measured in units of $g = 981\text{cm}^2/\text{sec}$. The fluid’s kinematic viscosity, ν is measured in cS ($0.01\text{cm}^2/\text{s}$), and the depth of the fluid layer h , is measured in cm. In many cases, we will identify, for simplicity, angular frequencies (e.g. ω) with the corresponding temporal ones (e.g. $\omega/(2\pi)$). Where necessary, angular or temporal frequencies will be explicitly denoted. Additional notation will be defined as needed.

B. Linear analysis

The linear stability analysis of the problem was performed by Besson et al. [13] by numerically solving the linearized Navier-Stokes equation via an extension of the technique developed by Kumar and Tuckerman [14] for single frequency excitations. As in the single frequency case, the acceleration-wavenumber plane is characterized

by alternating tongues corresponding to the acceleration at which a given wavenumber becomes linearly unstable. For mixing angles $\chi = 0^\circ$ and $\chi = 90^\circ$ the tongue structure of single frequency forcing with either $m\omega_0$ or $n\omega_0$ driving is obtained. Increasing χ from 0 results in the appearance of additional tongues whose dominant frequencies are spaced $\omega_0/2$ apart, since the system’s basic frequency is then ω_0 . Each odd numbered tongue possesses a *subharmonic* temporal dependence composed of only frequencies $\omega_0(p + 1/2)$ whereas even-numbered tongues are temporally *harmonic* i.e. composed of frequencies $p\omega_0$ (where p is any whole number). Although the time dependence of each tongue is given by an infinite series, the *dominant* frequency of the p^{th} odd (even) tongue corresponds to $(p + 1/2)\omega_0$ ($p\omega_0$). Generally, within the critical tongues the dominant frequencies $n\omega_0/2$ or $m\omega_0/2$ have an order of magnitude greater amplitude than the other components. Thus, the temporal response of the critical modes for $m/n = \text{odd/odd}$ driving ratios is always subharmonic. For odd/even (even/odd) the k_1 “tongue” has a subharmonic (harmonic) response while the k_2 has the opposite parity.

The system’s critical wavenumber, k_c , corresponds to the lowest acceleration, a_c , at which the flat, featureless state loses stability. At a critical value of $\chi = \chi_c$, a codimension 2 point exists where two tongues having wavenumbers k_1 and k_2 corresponding, respectively, to $m\omega_0/2$ and $n\omega_0/2$, simultaneously become unstable. For χ far from χ_c the critical wavenumbers are close to the values of k_c obtained for single-frequency experiments. Near the codimension 2 point k_c tends to differ from the corresponding single-frequency value by up to 10%. The calculated values of both a_c and k_c are in excellent agreement with experiments [13,15]. While modes other than the critical ones are linearly damped, we will see that they can play an important role in nonlinear wave interactions.

C. Experiments with two-frequency forcing

In the case of single-frequency driving, the subharmonic time dependence prohibits quadratic terms in the “amplitude” equations describing the nonlinear interactions between the amplitudes of the excited modes. However, when using two-frequency driving with odd/even or even/odd parity, both harmonic and subharmonic temporal responses are possible. When one of the driving frequency components is dominant, one can consider the smaller component as a perturbation that breaks the system’s temporal subharmonic symmetry. The reflection invariance of the corresponding set of coupled amplitude equations is then broken and, generically, quadratic terms can appear. These quadratic terms are important since they enable three-wave interactions between different modes.

Edwards and Fauve were the first to study the two-frequency driven Faraday instability [16–18]. They chose to focus most of their study on 4:5 driving although they also explored other ratios (such as 6/7, 4/7, 8/9 and 3/5). These experiments used a relatively viscous fluid and small fluid layer height in order to minimize lateral boundary effects. As the viscosity of the fluid was rather high ($\nu = 100$ cS) stripe patterns occurred for single-frequency driving. The phase space as presented in [16] for (even/odd) 4:5 driving can be divided into two parts: The harmonic (subharmonic) part where the k_1 (k_2) wavevector is dominant and the leading temporal term has the frequency of $4\omega_0/2$ ($5\omega_0/2$). In the harmonic region, in place of the stripe patterns of wavenumber k_1 appearing for pure $4\omega_0$ driving, a first order transition to hexagons occurs for $\chi > 10^\circ$. In the subharmonic region, striped patterns with wave number k_2 are observed until the near vicinity of the codimension 2 point at χ_c . The first-order transition to the hexagonal state results from the quadratic interactions mentioned above.

In the neighborhood of the codimension 2 point, a temporally harmonic, twelvefold symmetric quasi-periodic pattern was observed. These states appeared for only a small range of ϕ ($\phi \sim 75^\circ \pm 5^\circ$). They evolved, via a first-order bifurcation, from either the flat zero-amplitude state or the subharmonic striped patterns. In the hysteretic region of these states, Edwards and Fauve also observed solitary axial waves that originated from the quasi-periodic pattern. Arbell and Fineberg [19] have shown that these highly localized waves are related to “oscillons” states observed [20] in driven granular systems.

Muller [12] later conducted two-frequency forcing experiments using a 1/2 driving ratio. These experiments were performed near χ_c in shallow fluid layers in various regions of the $\chi - \phi$ phase space. Both temporally subharmonic hexagon and triangle patterns were observed. Triangular patterns are formed when the spatial phase associated with each of the excited eigenmodes differs from 0° or 180° . Muller showed that amplitude equations with both cubic and quintic terms (applying to temporally subharmonic waves), can form triangular patterns. In contrast, amplitude equations with quadratic terms have only stable hexagonal solutions. These experiments were later modelled by Zhang and Vinals [11] using a quasipotential approach. Experimentally, Muller showed that the addition of a third small-amplitude forcing frequency (which is equivalent to perturbatively breaking the system’s parity) could stabilize either the hexagonal or triangular states.

More recent experimental studies in 2 frequency-forced systems were performed by two groups, Kudrolli, Peir and Gollub [21] and Arbell and Fineberg [15,19,22]. These studies were conducted both in the near vicinity and far from χ_c . They revealed a number of qualitatively new, superlattice-type states in which new scales, not di-

rectly introduced via the external forcing, were evident.

In regions of phase space that can be relatively far from χ_c , superlattice states were observed as secondary bifurcations from the harmonic ($m\omega_0/2$) hexagonal states that occur for odd/even or even/odd driving ratios. The primary hexagonal symmetry with wavenumber k_c is broken by additional modes with wavenumbers $q < k_c$ whose temporal response possesses an $m\omega_0/4$ component. These states include “SL-II” states observed for 4:5 driving by Kudrolli et al. [21] and the Subharmonic Superlattice (“SSS”) states observed for a large number of driving ratios by Arbell et al. [15].

A second type of superlattice state is observed in the near vicinity of the codimension 2 point, once again on the side dominated by the *harmonic* driving component when even/odd or odd/even forcing is used. Two variants of these states coined “SL-I” [21] and double hexagonal states (“DHS”) [19] have been observed. These states can be described by the superposition of two hexagonal sets of wavevectors of magnitude k_c . The two sets of six wavevectors are oriented at an angle $\theta_r \simeq 22^\circ$ to each other. This specific angle is not arbitrarily chosen. The sum and difference vectors between the two wavevector sets produce a sublattice, spanned by the smaller difference wavevectors. When the two sets of wavevectors are oriented at specific angles of θ_r , the sublattice formed by the difference vectors becomes commensurate with the two hexagonal lattices. This structure is one of the generic possibilities that were anticipated on the basis of symmetry arguments proposed by Silber and Proctor [23].

A qualitatively different type of superlattice occurs in the vicinity of χ_c for all driving ratio parities. These states, coined 2-mode superlattices (2MS) [15], are the most general of the superlattice states observed. They are formed by an interaction of the two linearly excited modes (k_1 and k_2) with a third linearly-damped slaved mode that is nonlinearly excited. The angle between k_1 and k_2 is chosen by the following resonance mechanism: the vector difference $\vec{k}_2 - \vec{k}_1$ produces a third wavevector \vec{k}_3 . The magnitude of k_3 is determined by the dispersion relation, $\omega(k)$, for the difference frequency $\omega_3 = \omega_2 - \omega_1$.

An additional type of superlattice state has been observed for 2/3 and 4/5 driving in the vicinity of χ_c [22]. This state, which appears in place of the 2MS state, consists of a rhomboid pattern that is formed by the simple nonlinear resonance: $\vec{k}_2 - \vec{k}'_2 = \vec{k}_1$ where $|\vec{k}_2| = |\vec{k}'_2|$. When the coupling angle θ ($\theta \equiv \cos^{-1}[\vec{k}_2 \cdot \vec{k}'_2/k_2^2]$) between \vec{k}_2 and \vec{k}'_2 is tuned to a value of $\theta \sim 2\pi/n$, 2-n fold quasicrystalline patterns are naturally formed.

D. Model equations and nonlinear analysis

Generally, two methods have been used to study the Faraday instability with two-frequency driving. The first uses simple model systems that yield qualitative insights regarding the behavior of the Faraday system. These use general assumptions based mainly on symmetry considerations. The second method is to start from the full nonlinear set of equations that describe the system, employ carefully chosen approximations, and derive a set of equations that describes the behavior of the system based on the real physical parameters. Both methods have yielded valuable insights.

1. Model equations

The observation of quasi-crystalline patterns (“quasi-patterns”) generated using two-frequency driving by Edwards and Fauve [16] and via single frequency driving by Binks et al. [24] provided a motivation to find model equations that display similar behavior. Muller [25] first considered a system of N coupled Landau equations with cubic nonlinear terms. These equations could be written as the gradient of a Lyapunov functional. Muller showed, by minimization of this functional, that regular N -fold patterns of different symmetries can be stable. Pattern selection depended on the value of the nonlinear coefficients coupling the linearly degenerate modes. This mechanism may be related to both the appearance of quasi-patterns in single frequency Faraday experiments and to the quasi-patterns observed in the harmonic region of two-frequency Faraday systems with even/odd driving.

A second mechanism that can create quasi-patterns is related to quadratic interactions between degenerate nonlinear modes. Muller proposed that a quadratic nonlinearity, generating the triad interaction: $\vec{k}_2 - \vec{k}'_2 = \vec{k}_1$ ($|\vec{k}_2| = |\vec{k}'_2|$) could also lead to quasi-crystalline patterns. The angle between \vec{k}_2 and \vec{k}'_2 is tunable by the ratio k_1/k_2 , with resonant angles $\theta = 45^\circ$, $\theta = 36^\circ$, $\theta = 30^\circ$ for 8-fold, 10-fold and 12-fold quasi-patterns respectively. These states were observed in a system of two coupled Swift-Hohenberg equations, each with a different unstable wavenumber. Frisch and Sonnino [26] also observed subcritical 10-fold symmetrical patterns in coupled Swift-Hohenberg equations. This state was numerically shown to be stable even when the dynamics are not derived from a free energy functional. In addition to states with N -fold symmetry, nonsymmetric, rhomboidal patterns were also seen to be stable for some parameter values. Later, both the rhomboidal patterns and resonant quasipatterns resulting from the above interactions were observed experimentally by Arbell and Fineberg [22].

Lifshitz and Petrich [27] modeled the two-frequency Faraday system with a single generalized Swift-Hohenberg type equation for a *single* real field $u(x, y)$. This model is simpler than the coupled equations used by Muller, Frisch and Sonino, and Newell and Pomeau [28]. The model equation used was rotationally invariant with *two* built-in critical wavenumbers. The equation contained a quadratic term that both broke the system’s up-down symmetry and allowed triad wave interactions. Stable striped, hexagonal and 12-fold symmetric patterns were observed for different values of the control parameter. In addition to these N -fold symmetric states, a compressed hexagon state, similar to the rhombic/stripe pattern described by Muller, was observed.

The above model systems suggest that the existence of two unstable wavenumbers together with the possibility of triad interactions (provided by quadratic terms) is a sufficient condition for the formation of quasi-periodic patterns. Another common feature of these models is the existence of distinct regions of phase space in which patterns that lack N -fold symmetry are stable.

2. Nonlinear analysis

In contrast to the simplified model systems described above, Zhang and Vinals [11] derived a description of the system’s dynamics from the governing equations for the 2-frequency Faraday problem. To this end, they applied the quasi-potential approach developed for single-frequency study [29] to the problem of two-frequency driving. This approach is strictly valid in the limits of weak dissipation and infinite fluid depth.

To compare their results with Muller’s experimental results, Zhang et al. analyzed the special case of 1/2 driving in depth. They first used the linearized equation to study the location of the codimension two point, χ_c as a function of the phase difference ϕ . The results were in qualitative agreement with the experiments. The discrepancies were attributed to the high damping used in Muller’s experiment, which was outside the region of validity of the theory. It is interesting to note that the dependence of χ_c on ϕ is a special feature of 1/2 driving and does not occur for other driving combinations.

Zhang and Vinals then, using a multiple scales approach, derived standing wave amplitude equations. This weakly nonlinear analysis assumed that the system was far from the codimension 2 point, so that a single temporal mode dominated the dynamics. For the case of 1/2 driving, they first obtained a prediction for the relative magnitudes of the different Fourier components of the weakly nonlinear temporal response of the fluid surface. Then, assuming N degenerate modes, the coupled amplitude equations describing these modes were derived. In contrast to [25], the function $\beta(\theta_{ij})$ coupling the i^{th} and j^{th} modes, was computed from the physical parameters

of the problem. One interesting result of this calculation was that the phase difference ϕ can have a strong effect on the coupling function β - and thereby a strong effect on the nonlinear pattern selection. The relative stability of different N-fold nonlinear states was then calculated by minimization of a Lyapunov functional, as in [25] and [27]. Semi-quantitative agreement with the regions of stability observed experimentally in [12] for different patterns (squares, hexagons/triangles and quasi-patterns of various orders) observed in the *subharmonic* region of the $\phi - \chi$ phase space was obtained.

An important result of this work was that it suggested a new type of physical mechanism that governs the selection process. These calculations indicated that the value of the coupling coefficients was strongly influenced by triad interactions between the linearly excited modes (corresponding to the dominant excitation frequency) and the *linearly stable* modes corresponding to the *second* excitation frequency. Resonant coupling to these latter modes served, in the region of phase space far from χ_c , to enhance the effective damping - as energy transferred to these “slaved” modes is more efficiently dissipated. Far from χ_c , states that can *not* couple to the slaved modes are then preferred by the system. As we shall later see, however, in the *vicinity* of χ_c resonant triad coupling to the linearly stable, slaved modes provides one of the main mechanisms for the rich variety of nonlinear states observed.

Silber and Skeldon [30] were the first to theoretically study the two-frequency Faraday system in the vicinity of the codimension 2 point. This study pointed out the importance of accounting for the temporal symmetries of the system. Silber and Skeldon focused on forcing ratios, m/n , having either odd/even or even/odd parities, where interactions between harmonic and subharmonic waves may occur.

As shown in [11], resonant mode interactions greatly affect the mode coupling function $\beta(\theta)$. Using normal form analysis, Silber and Skeldon showed that triad resonances $\vec{k}_1 \pm \vec{k}'_1 = \vec{k}_2$ (where $k_1 = k'_1$) are only possible when the temporal mode corresponding to k_2 is *harmonic*. When k_2 has a subharmonic temporal dependence, quadratic terms in normal form equations can be eliminated [31,32] - thereby decoupling the harmonic modes from the subharmonic ones. This can be simply understood since the product of two linear eigenfunctions (resulting from a quadratic interaction term) results in the addition of their temporal phases. The sum of *two* harmonic or subharmonic temporal phases cannot produce a subharmonic one, therefore two modes of like parity cannot couple quadratically to a subharmonic state. Silber and Skeldon [30] went on to demonstrate the above, by calculating the amplitude equations for both 1/2 (odd/even) or 2/3 (even/odd) driving by means of the quasi-potential approximation used in [11].

The existence or suppression of three wave resonances can have a significant effect on the qualitative features of the phase diagram. When one is far from χ_c we have seen [11] that three-wave resonant coupling influences pattern selection by enhancing dissipation via the coupling to a heavily damped (slaved) mode. In this case, resonant triads are strongly *suppressed*. On the other hand, when in the near vicinity of χ_c , resonant coupling to nearly unstable linear modes can occur. Moreover, if these modes undergo a first order bifurcation, their growth will be (to first order) unchecked and resonant coupling to them may have a very significant effect on the spatial-temporal behavior of the system.

Silber, Topaz and Skeldon [33] have recently demonstrated the importance of resonant coupling to slaved modes for 6/7 forcing near χ_c . Using the quasi-potential approximation [11] they showed how weakly damped linear modes with wavenumbers $K < k_c$, quadratically couple to the unstable modes to create the “SL-I” states observed by Kudrolli et al. [21]. In this case, the critical wavevectors $|\vec{k}_i| = k_c$ could be constructed from a commensurate hexagonal sublattice of wavevectors, \vec{K}_i , such that $\vec{k}_i = q\vec{K}_1 + p\vec{K}_2$. The “SL-I” states are a particular case where $(p, q) = (\pm 2, \pm 3)$ with $k_c/K = \sqrt{7}$. This particular coupling was made possible by the existence of a weakly damped linear “tongue” with a wavenumber close to K . The “SL-I” state was *not* observed for 2/3 forcing since, for this forcing ratio, no linear tongues near this resonance exist since there are no additional harmonic modes with $K < k_c$ (K_i must be harmonic by [30] as they result from the vector difference of two \vec{k}_i modes).

Recent work by Tze, Rucklidge, Hoyle and Silber [34] has shown that the “SL-II” states observed by Kudrolli et al. [21] may be understood as resulting from a symmetry-breaking bifurcation of an initial hexagonal symmetry. Study of the possible invariant subgroups of the original $D_6 + Z^2$ symmetry characterizing hexagonal standing waves revealed a number of possible solution branches. One of these corresponds to the spatial symmetry of temporally-averaged “SL-II” type states. Depending on the normal form coefficients, 5 additional possible solution branches were predicted. It remains to be seen whether these other branches are experimentally observed.

II. EXPERIMENTAL SYSTEM

Our experimental system consisted of a shallow fluid layer, laterally bounded by a plastic sidewall and mounted on a computer-controlled mechanical shaker. A 1 cm thick, black-anodized aluminum plate of 14.4 cm diameter supported the fluid from below. This plate was machined to a $10\mu\text{m}$ flatness. The mechanical shaker used (either Unholtz-Dickie model 5PM or VTS model

100) provided vertical accelerations ranging from 0 to 15g. The cell acceleration, regulated to within 0.01g, was monitored continuously by a calibrated accelerometer (Silicon Designs, INC 1210L-010) attached directly to the armature of the shaker. A feedback mechanism was used to control and stabilize the amplitude A , mixing angle χ , and phase ϕ to desired values.

Most of our experiments were conducted with Dow Corning 200 silicone oil of different viscosities (DC200/10, DC200/20, DC200/50 and DC200/100). Silicone oil has a typical density of 0.95 gr/cm³ and surface tension of 21.5 dyne/cm. This fluid is Newtonian for the viscosity range of 1–100 cS. Since the fluid viscosity is highly temperature dependent, stabilizing the fluid temperature was important. A stable fluid temperature of $30 \pm 0.05^\circ\text{C}$ was used in all experiments. Resultant viscosity variations were less than 0.04 cS. A number of experiments were also performed using TKO-77 vacuum pump fluid with viscosities ranging between 221 cS at 33° and 184 cS At 30°. Both Dow Corning 200 and TKO-77 have very low vapor pressures so there was no need to seal the cell against evaporation. The results of our experiments showed no dependence on the particular type of fluid used.

Our experiments were performed at frequencies between 20-150 Hz. The selection of the frequency was influenced by the aspect ratio of the patterns and the shaker's maximum acceleration and stroke. Frequency selection was also influenced, to a lesser extent, by limitations of the imaging and laser probe technique. Typically the aspect ratio between the cell diameter, L , and the wavelength λ , was between $5 < L/\lambda < 50$. The maximal driving frequency of 150 Hz was governed by a_c , which increases with increasing ω . The shaker's maximal stroke (2.5 cm peak to peak) and boundary mode quantization at small aspect ratios dictated the lower frequency limit.

A. Boundary Conditions

The lateral boundary conditions of the experimental cell can have an important effect on the waves excited by the system. In our experiments we attempted to minimize the role of the sidewalls. A circular shape for the lateral boundary was chosen. This ensured that no particular pattern was preferred. This is especially significant when the system is only slightly dissipative (e.g low viscosity fluids and/or large fluid depth). For a more highly dissipative system (e.g high viscosity fluids and/or shallow fluids), the boundary's shape does not influence the symmetry of the excited pattern [18].

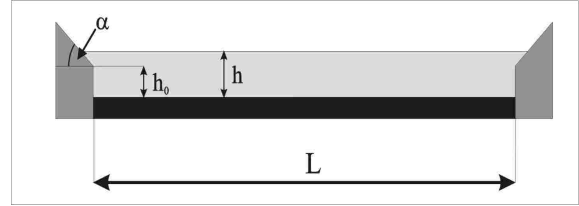


FIG. 1. (top) A profile of the container used is shown: a Delrin circular boundary (gray) is attached to the bottom plate (black). The boundary consists of a vertical section of height h_0 and an inclined section at an angle of $\alpha = 20^\circ$ chosen to allow the surface of the liquid used, Dow Corning 200, to be at zero contact angle with the rim (liquid in light gray). Rings with h_0 of 1 mm, 1.5 mm, 2.5 mm, 4 mm and 5 mm were used. h could be changed continuously by adding small amounts of fluid with a calibrated pipette.

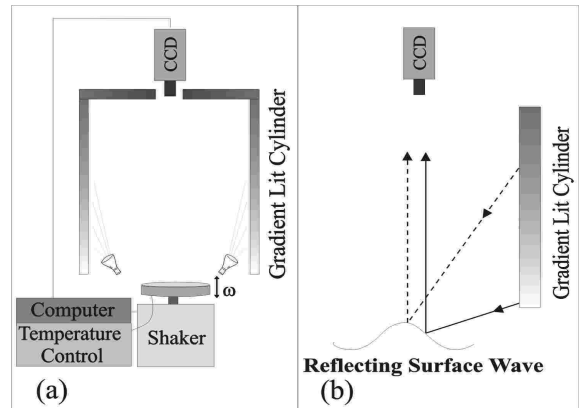


FIG. 2. (a) A schematic diagram of the experimental system. The imaging system consisted of a cylindrical screen, concentric with the experimental cell, which was illuminated by halogen lamps arranged in a circle. A CCD camera was mounted on the cylinder axis above the fluid surface. (b) The cylinder's illumination intensity was varied as a function of the height above the fluid. At each point on the fluid surface the local slope reflects only a single point from the cylinder surface into the CCD. Since the lighting provides a unique intensity at each height along the cylinder, the intensity reflected by each point is uniquely mapped to the projection of the fluid surface's slope in the direction of the cylinder axis.

As discussed by Douady (1990) [1], an additional effect of sidewalls is the possible emission of waves (meniscus waves) from the lateral boundaries. These waves are forced at the driving frequency via forced height variations of the meniscus formed at the contact line between the fluid and lateral boundaries. Meniscus waves have no threshold and can therefore mask the instability threshold of parametrically forced waves. To minimize this effect, our system's lateral boundaries (shown schematically in Fig 1) were sloped at an angle conjugate to the contact angle between the fluid and the material (Delrin) from which the lateral rings were constructed. (A slope

of $\alpha = 20^\circ$ was used for the Dow Corning 200 silicone oil.) In this way, we ensured that the static fluid interface was nearly flat.

An additional advantage of sloped lateral boundaries is the elimination of reflected waves by impedance matching. Since the instability threshold increases with decreasing h , a gradual decrease (sloping sides) in fluid depth increases the effective local threshold at the larger radii to far beyond a_c . Since the typical height of the fluid layer in the sloped region was only 0.1 – 0.8mm, parametric waves could not be excited and any meniscus waves emanating from the wall were strongly damped. In practice, this boundary condition combined with the fluid viscosities and depths used enabled us to obtain values of a_c within 2% of the calculated values [35,13,36] for a system of infinite lateral extent.

B. Visualization

1. Imaging from above

To visualize the fluid surface, we employed a novel imaging technique. The imaging system is schematically shown in Figure 2b. The experimental cell was illuminated by a tall cylindrical screen whose axis was concentric with center of the cell. The screen was illuminated from below by a ring of 12 small lamps. As a result, the light intensity along the screen varied as a function of the height above the fluid. A CCD camera was mounted on the cylinder axis, 1.4m above the cell. At each point on the fluid surface (see Figure 2b), the local slope reflects only a single point from the screen onto the CCD. Since the lighting provides a unique intensity at each height along the cylinder, the intensity reflected by each point on the fluid surface is uniquely mapped to the projection of its slope on the cylinder axis. We used the CCD's high speed shuttering mode (1/1000 sec) to obtain instantaneous images of the fluid surface.

Two methods of triggering were used to control the CCD camera. The first method employed a trigger signal that was synchronized with the driving. This signal both reset the camera and initiated acquisition of the video frame at a desired phase relative to the driving signal. To observe slow changes in the patterns over long times, slow trigger rates that were commensurate with the driving frequency were used. The short-term behavior of a state in its different temporal phases was studied by the use of slightly incommensurate trigger rates. This allowed nearly continuous acquisition of the different temporal phases of a given state without the need for very high-speed acquisition.

Our imaging technique, although providing quantitative information, does not directly yield the surface wave height function $h(x, y)$. The imaging yields a grayscale

image, $I(x, y)$, that is approximately the absolute value of the gradient of the height function i.e.

$$I(x, y) = \sqrt{(\partial_x h(x, y))^2 + (\partial_y h(x, y))^2} \quad (2)$$

One must then work backwards from $I(x, y)$ to determine the function $h(x, y)$. This is done by inputting an assumed state into Eq. 2 and comparing the computed pattern to the state observed. By iteration it is possible to arrive at fairly good estimates of $h(x, y)$. Some examples are presented in Figure 3.

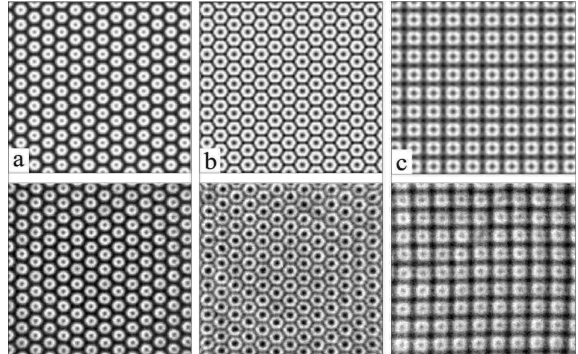


FIG. 3. Using the method described in the text we calculated model images (upper) of a simple hexagonal state in its peak state (a) and crater state (b) and of a square state (c). The corresponding experimental patterns are shown (bottom). To model the surface waves we assumed an asymmetry between up hexagons and down hexagons due to the fact that the hexagon's amplitude was large compared to the small layer height.

For high-amplitude states, visualization from the side was sometimes used. This was performed by illuminating from the side and placing a video camera in the horizontal plane of the plate at the height of the system's lateral boundary. This configuration enabled direct quantitative measurements of the wave amplitudes adjacent to the lateral boundaries of the cell. An additional advantage of this imaging was that it allowed us to simultaneously view both the lower plate's vertical movement together with the wave's motion. In this way their relative phase could be directly measured.

C. High resolution temporal measurements

Most previous studies of the Faraday system have used imaging techniques that mainly yield information about the symmetries of the states observed. Time domain information was generally extracted by the use of stroboscopic lighting at the frequency of the shaker. This technique measures the lowest frequency in which a state oscillates but yields no information about higher harmonics. Two experimental studies used a laser beam probe to extract information about the surface waves. Douady [1]

used a laser beam deflected at an angle from the surface waves and reflected on a screen to study the amplitude of the waves. Gollub and Simonelli [37] used a laser beam deflected from the surface waves onto a photo detector to obtain temporal information. This technique, however, could not give precise information about the slope of the fluid surface since an average intensity reflected from a single “cell” of the pattern was measured.

We combined these two methods by imaging the reflection at the fluid surface of a highly focused laser onto a position sensitive detector (UDT SL20). This method yielded an accuracy of 1 – 5% in the surface slope and a temporal resolution of 0.02 mS. Good signal to noise was obtained by amplitude-modulating the laser signal and then deconvolving the resultant signal of the position sensitive detector (PSD). The temporal response of the system was only limited by the maximal sampling frequency of the PSD voltage.

III. OVERVIEW OF THE PHASE DIAGRAM

The phase space of the two–frequency Faraday system is very large. Besides physical parameters such as fluid layer height and viscosity, one also has to set the driving parameters. Introducing two driving components with different frequencies, different amplitudes and a nontrivial relative phase makes the task of choosing a working regime and the relevant dimensionless combinations of parameters a difficult one.

We have chosen to focus on the simplest commensurate driving ratios as a first step. The m/n ratio combinations used in our experiments were numerous: 1/2, 2/3, 2/3, 2/5, 2/7, 3/4, 3/5, 3/7, 4/5, 4/7, 5/6, 5/7, 5/8, 6/7, 6/11, 41/60, 40/59, 21/50. Most of our detailed experiments were performed with no phase difference between the two frequency components ($\phi = 0$ in Eq. (1)). For system parameters that were seen to excite special patterns, scans of ϕ were made. Changing ϕ was found to be crucial for the existence of some of the states and of no relevance to others. Phase diagrams were constructed by fixing the mixing angle χ and increasing the amplitude A until a state of droplet ejection was reached.

Two typical two–frequency phase diagrams for even/odd driving are presented in Figure 4. In single frequency experiments rolls, squares, hexagons and quasipatterns of different symmetries are known to exist depending on the viscosity, height, frequency and amplitude above the threshold. In our parameter regime, the dominant structure in regimes dominated by a single frequency is squares for low viscosities ($\nu = 8.7 - 23$ cS) and both squares and rolls for higher viscosities ($\nu = 47 - 87$ cS). As in other studies of two–frequency driving [12,16,17], two main regions, dominated by either k_1 or k_2 , exist. Each of these regions has not only a different wavelength but also different temporal behavior.

The k_1 and k_2 dominated regions have a strong response at $\omega_1/2$ and $\omega_2/2$ respectively. This is true for all values of m/n . The temporal response, however, consists of additional frequency components that depend on the ratio m/n . When both m and n are odd (odd/odd driving) the excited surface modes in both regions of phase space have only subharmonic components (i.e. $(p+1/2)\omega_0$ with p an integer). In the case of odd/even (even/odd) driving, the k_1 dominated region is temporally subharmonic (harmonic) while the k_2 dominated regime is temporally harmonic (subharmonic). At the critical value $\chi = \chi_c$, a codimension 2 point exists where both wavenumbers are simultaneously linearly unstable. The k_1 dominated region occurs for $\chi < \chi_c$ while the k_2 dominated region occurs for $\chi > \chi_c$. The interaction of k_1 and k_2 leads to a variety of different nonlinear states in the vicinity of χ_c . Before describing these states, we will first describe the effects of two–frequency driving in the two main regions far from χ_c .

In the regions dominated by harmonic states we have found a number of non–trivial states that bifurcate from single–mode hexagonal states while breaking both their spatial and temporal symmetries. These symmetry–breaking bifurcations can even occur when χ is quite small. The subharmonic superlattice state (SSS) (Figure 4 (bottom)) is an example of such a symmetry breaking state. SSS states are formed in the k_1 dominated regime with $\chi_c - 5^\circ \geq \chi \geq 10^\circ$, when the primary hexagonal state’s symmetry with *harmonic* temporal behavior is broken by an additional set of wavevectors of magnitude $q < k_1$ with *subharmonic* temporal behavior (frequency $\omega_1/4$) with respect to the primary $\omega_1/2$ frequency. We have observed two main types of SSS states, which differ from each other in the orientation, magnitude and number of \vec{q} wavevectors. For example, the SSS state shown in Figure 4, (SSS type I) breaks the initial hexagonal symmetry by the introduction of two wavevectors \vec{q} , which are parallel to two of the three initial wavevectors \vec{k}_1 . The magnitude of q in this case is $k_1/2$ which yields a simple resonance condition $\vec{q} + \vec{q} = \vec{k}_1$. SSS have been observed only for even/odd driving for *all* of the m/n combinations listed above. The different SSS types and the mechanisms that form them will be described in detail in Sec. IV

For even/odd driving, the effect of two frequency driving on the pattern formation in the k_2 dominated region is quite different than in the k_1 dominated region. In the k_2 region, square symmetry dominates at threshold from $\chi = 90^\circ$ to $\chi \approx \chi_c$. Only in the vicinity of χ_c do we see the effects of the two–frequency driving on the patterns formed. It is interesting to note that although theory predicts that hexagons are preferred for harmonic response and squares for subharmonic response (see Sec. I), we have observed *square* symmetry in large parts of the harmonic region for odd/even driving ($\chi > \chi_c$).

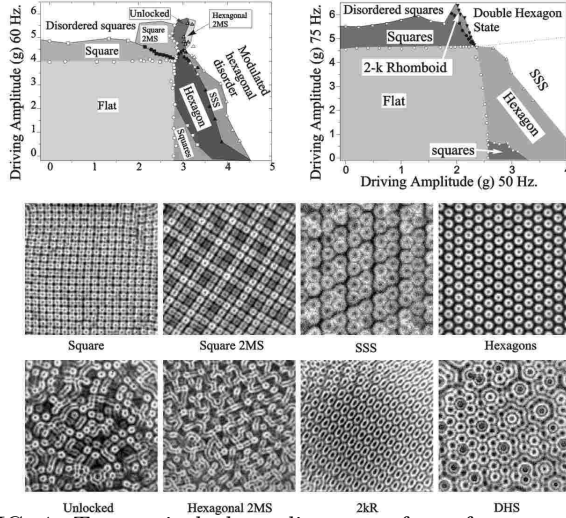


FIG. 4. Two typical phase diagrams of two-frequency experiments obtained for 2:3 driving with different system parameters: $\omega_0 = 20$ Hz and $h = 0.155$ cm (left) and $\omega_0 = 25$ Hz and $h = 0.2$ cm (right). In both experiments $\nu = 23$ cS and $\phi = 0^\circ$. Square regions exist in the near vicinity of single frequency forcing. The square symmetry dominates in the subharmonic regime to near χ_c while throughout most of the harmonic region the hexagonal symmetry dominates. In the vicinity of the co-dimension 2 point we observe three new states that exist for many combinations of the driving ratio. These states are 2 mode superlattices (2MS), with underlying square or hexagonal symmetries and spatially and temporally unlocked states (“Unlocked” states). A resonant state that consists of a rhomboid unit cell ($2kR$) was also observed (right). Unlike the 2MS and unlocked states, which appear for many different driving ratios (odd/odd, odd/even and even/odd), this state was observed for only for 2/3 and 4/5 driving. In the harmonic region of phase space where hexagons are initially dominant, a second bifurcation occurs to either temporally subharmonic states (Subharmonic Superlattice State, SSS) or high amplitude waves (as well as, at times, localized “oscillon” waves) that appear on a double hexagonal superlattice (DHS). Symbols in the phase diagram describe measured transitions for fixed χ . (bottom) Typical photographs of these states.

Let us now briefly describe the patterns formed for even/odd driving in the vicinity of χ_c . Starting with the k_1 dominated ($\chi < \chi_c$) region, two types of patterns are observed near χ_c . One pattern, which we call the “Double Hexagonal State” (DHS) is formed by two sets of hexagonally arranged wavevectors (of length k_1) with a finite angle, α , between them. In the phase space shown in Figure 4, $\alpha \sim 22^\circ$. In contrast to the SSS, this state does *not* break the temporal symmetry of the harmonic hexagon state. Depending on various system parameters, DHS are sometimes formed by a first-order bifurcation. Perhaps their most outstanding characteristic is their very high amplitude. The surface wave maxima can reach amplitudes much higher than the fluid layer’s

height. In [19] we have shown how the DHS states can form oscillons, a highly localized large-amplitude nonlinear state that has been observed [19,20,38] in a number of periodically driven systems.

A special case of the DHS occurs for $\alpha = 30^\circ$, whence one obtains 12-fold quasipatterns such as first observed in [16]. We have seen the formation of such patterns for 4/5 driving in the same region where the DHS with $\alpha = 22^\circ$ appears for 2/3 driving.

Let us now move to the vicinity of χ_c both on the border of the k_1 region and within the k_2 region. Here two linearly unstable eigenvectors with different magnitudes can be concurrently excited. There are numerous possible configurations in which such a system can organize itself. Four different classes of mixed mode states were found to exist. These will be described in detail in Section VI.

- *Two mode superlattices (2MS)* These states formed by the interaction of the dominant mode (e.g. k_2) with its original symmetry and the weaker mode (e.g. k_1), which breaks the symmetry of the original pattern. The symmetry of the dominant mode can be either square or hexagonal depending on the proximity of the nearest primary state in phase space. In Figure 4 we present two types of 2MS modes, a square 2MS obtained for $\chi > \chi_c$ and a hexagonal 2MS obtained for $\chi < \chi_c$. The temporal behavior of the 2MS contains both the $\omega_1/2$ and $\omega_2/2$ frequency responses and always includes the subharmonic frequency of $\omega_0/2$. These states appear for all types of driving (odd/even, even/odd and odd/odd) although the precise structure of phase space depends on the driving ratio used.
- *Unlocked States* Between the square and hexagonal 2MS states an intermediate region exists where both k_1 and k_2 appear but no well-defined symmetry or spatial mode locking is observed. Thus, no long range correlations in either space or time exist. The basic time scale of the surface waves is $T = 4\pi/\omega_0$ but the pattern changes its local structure over time scales of order $(10^2 - 10^3)T$.
- *Rhomboidal states* Changing h , ν or ω_0 can lead to qualitative changes in the phase space. Figure 4 shows two different phase diagrams obtained for 2/3 driving. The only difference between the two diagrams is the fluid layer height and the value of basic frequency ω_0 . Lioubashevski et al. [39] describe how the dimensionless number δ/h , defined by the ratio between the effective boundary layer depth, $\delta = \sqrt{\nu/\omega_0}$, and the fluid height, h , affects single mode states selected by the system. For a certain range of δ/h rhomboidal patterns replace the 2MS and unlocked states (see Figure 4 bottom). These states couple two wavevectors of

length k_2 with one wavevector of length k_1 . These wavevectors evolve *spontaneously* from two circles of linearly degenerate states. We will show that for special parameter values, n -fold quasipatterns can naturally evolve from the rhomboidal structures.

In addition to the states described above, in Section VIII we will show examples of a number of other resonant structures that are formed for different system parameters. The richness of this system allows one to observe a wide variety of different resonant patterns. We will show some common traits of these resonant selection mechanisms that can lead to a more comprehensive understanding of resonant interactions in pattern forming systems.

IV. SUBHARMONIC SUPERLATTICE STATES (SSS)

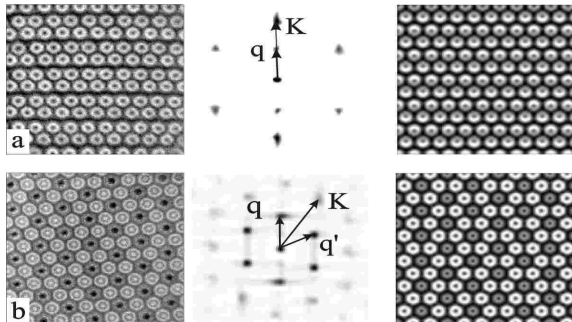


FIG. 5. For $2/3$ driving we observe two types of temporally subharmonic superlattices, the SSS-I (a) SSS-II (b). Experimental images (left) together with their spatial power spectra (middle) and simulated images (right) are shown. In (a) we see that a small vector of magnitude $q = K/2$ ($\vec{q} \parallel \vec{K}$) breaks the hexagonal symmetry formed by primary wavenumbers \vec{K}_i , where $K_i = k_c$. In (b) the primary hexagonal symmetry is broken by wavevectors $q = K/\sqrt{3}$ located at a 30° angle relative to the primary wavevectors. Both patterns can exist in regions far from χ_c , where the higher odd-frequency component is weak (see Figure 4). The patterns obey the resonance conditions $2\vec{q} = \vec{k}_c$ (SSS-I) and $\vec{q} + \vec{q}' = \vec{K}$ (SSS-II).

Hexagonal patterns can be formed in two-frequency experiments when the basic subharmonic temporal invariance is broken and quadratic nonlinear terms appear in the amplitude equations describing the system. These terms can occur in regions of the two-frequency phase space that have a harmonic response. By increasing the amplitude of the driving, the primary hexagonal symmetry can be broken and new *stable* structures appear even in regions where the second externally driven mode cannot be excited at all. In this section we will describe the characteristics of these symmetry breaking patterns.

In the notation used in this section, \vec{K} is the linearly unstable wavevector, excited $\omega_1 = m\omega_0$, that characterizes the primary pattern. \vec{q} is an additional smaller wavevector that appears in states that bifurcate from the primary pattern. Since in each pattern there is a degeneracy in the direction of the wavevectors, we will use an index to number the different wavevectors of the same magnitude e.g. \vec{K}_i $i = 1, 2, \dots$

Sub-harmonic superlattice states occur over a wide range of χ in the two-frequency phase diagram where the lower frequency, ω_1 , is dominant. SSS were observed for most even/odd frequency ratios tested, but were *not* seen for odd/even or odd/odd ratios. Since the first SSS type state was found [15] additional variants have been observed for different experimental parameters. Both types of SSS pattern, SSS-I (Figure 5a) and SSS-II (Figure 5b) are shown with their corresponding spatial power spectra. Both states share the following characteristics:

- The basic temporal dependence of both SSS types is subharmonic with respect to the the primary instability i.e. the system has a strong response at $m\omega_0/4$.
- These states are secondary bifurcations of temporally harmonic hexagonal states.
- Both states occur in the same basic region of phase space (for $0 < \chi < \chi_c$).
- In both states k_2 wavevectors are *not* observed.

The different states, in general, occur for different fluid parameters such as fluid viscosity, fluid depth and ω_1/ω_2 ratios. The most obvious differences can be seen in Figure 5. Examining their spatial power spectra, we see that while both SSS-I and SSS-II's spectra are constructed by three evenly spaced wavevector pairs, \vec{K}_i . The spectra include additional sets of wavevectors, \vec{q}_i (where $|q_i| < K$), of smaller magnitude. The orientations and magnitudes of \vec{q}_i *differ* in SSS-I and SSS-II states.

In SSS-I \vec{q}_i are oriented solely along (some or all of the) axes defined by the \vec{K}_i . The lengths of the q_i in the SSS-I are usually $K/2$, but in some cases the $q_i \neq K/2$.

SSS-II states are formed by a set of \vec{q}_i which *always* consists of three evenly spaced wavevector pairs of magnitude $q = K/\sqrt{3}$ arranged at an angle of 30° relative to the direction of the \vec{K}_i triad. The magnitude and orientation of q_i yield the simple resonance condition $\vec{q}_1 + \vec{q}_2 = \vec{K}_i$. While the SSS-I have been observed for a wide range of driving ratios ($2/3, 4/7, 2/5, 2/7, 4/5$), the SSS-II have only been seen for $2/3$ and $4/5$ driving. Both types of SSS states have recently been identified as representations of different invariant subgroups when hexagonal symmetry is broken [40,41].

In the next subsections we will present a detailed description of each of the SSS types together with a mechanism that can explain their formation.

A. Subharmonic Superlattice type I (SSS-I)

The spatio-temporal behavior of the SSS-I state can be modelled by a simple equation for the surface height function:

$$h(r, t) = \cos\left(\frac{1}{2}m\omega_0 t\right) \sum_{i=1}^3 A_i \cos(\vec{K}_i \cdot \vec{r} + \alpha_i) + \cos\left(\frac{1}{4}m\omega_0 t + \gamma\right) \sum_{i=1}^M B_i \cos(\vec{q}_i \cdot \vec{r} + \beta_i) \quad (3)$$

with

$$\vec{q}_i \parallel \vec{K}_i, \beta_i = 0, 90^\circ \quad (4)$$

where M is the number of axes with broken symmetry, γ is the *temporal* phase difference between the two sets of modes and α_i and β_i are the respective *spatial* phase of the \vec{K}_i and \vec{q}_i components. Because the pattern has hexagonal symmetry we assume $\alpha_i = 0^\circ$ and not $\alpha_i = 2\pi/3$ as in patterns having triangular symmetry [12]. Eq. 3 summarizes the most important features of the SSS-I in a compact way. We will now present experimental evidence for the validity of this equation and describe the relevance of each term (A_i , B_i , γ , β_i and M) in the experimentally observed states.

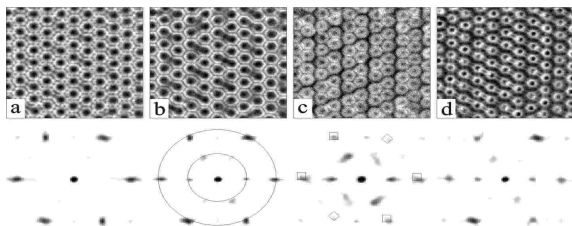


FIG. 6. Typical temporal sequences of an SSS-I state (a) taken at constant values of the driving parameters for the frequency ratio 40/60 Hz. The spatial Fourier spectra are composed solely of wavenumbers K , corresponding to $\omega_1/2$, and $q = K/2$. The *locations* of the peaks are fixed in the different temporal phases. For the system parameters $\omega_0/(2\pi) = 20$ Hz, $\nu = 23$ cS, $\phi = 0^\circ$, and $h = 0.155$ cm the hexagonal symmetry is broken in *two* directions by the $K/2$ vectors. Circles of radii K and $K/2$ are drawn in (b). The relative intensities of the different wavevectors can be seen; in (a) \vec{q}_i are nearly absent while in (c) their intensities are almost equal to the \vec{K}_i . The symmetry breaking is also revealed in the intensities of the primary hexagonal vectors, as can be seen in (c), where the two strong intensity wavevectors are enclosed in a square and the weak one in diamonds.

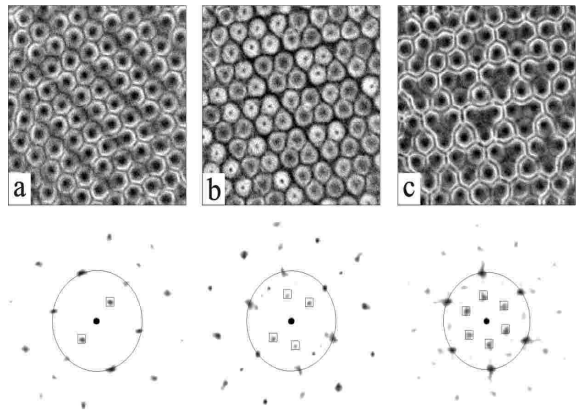


FIG. 7. Images (top) and power spectra (bottom) of an SSS-I type state with broken symmetry in one, (a) two, (b) and three (c) directions. The circles indicate the primary hexagon wavevector's magnitude, K . The symmetry breaking vectors of magnitude $q = K/2$ are enclosed in squares. All images were obtained for the same system parameters of $\nu = 23$ cS (40/70 Hz and $h = 0.155$ cm, $\chi = 43^\circ$ and $\phi = 0^\circ$). This pattern is not stable and drifts slowly (order of 10–60 seconds) between these three states.

In Figure 6 we present a sequence of SSS-I states taken at different times for constant values of the driving parameters. Although the state's appearance changes with time, their spatial Fourier spectra reveal that the state results from the interaction of two specific spatial scales; the primary wavenumber $|\vec{K}| = |\vec{k}_1|$ that is excited by the ω_1 frequency component, and its spatial sub-harmonic, $\vec{q} = \vec{K}/2$. The SSS spectra show that while the \vec{K}_i have 6-fold symmetry, two \vec{q}_i with relatively large amplitude and a third smaller amplitude \vec{q}_i have broken this symmetry. The amplitudes of the q_i vary with time. Within the temporal phases shown in Figure 6a the q_i amplitudes have little power while in Figure 6c the \vec{q}_i are stronger than the \vec{K}_i components. This behavior is reflected by the temporal phase, γ , in Eq. 3. The symmetry breaking is reflected by the relative strengths of both the \vec{q}_i and \vec{K}_i . It is clear that the two K wavevectors enclosed in squares, have different strength than the wavevector enclosed in diamonds. This symmetry-breaking is also seen in the relative power of the q_i wavevectors.

As demonstrated in Figure 7, SSS states can have broken symmetry in one, two or three directions ($M = 1, 2, 3$ in Eq. 3). In most cases, a specific number of symmetry breaking directions was selected. However, for the experiment described in Figure 7, the pattern drifted slowly (on the scale of seconds) between the three possible symmetry-broken states.

The transition between the primary hexagonal pattern and the SSS states is (within $\approx 1\%$) *non-hysteretic* and occurs via a circular front that propagates slowly inward from the plate's lateral boundaries. The process is continuous and reversible (see Figure 8). Before continuing

the study of the spatial characteristics of the SSS-I pattern let us digress briefly and examine the temporal behavior of the system using the laser probe method (see Sec. II C).

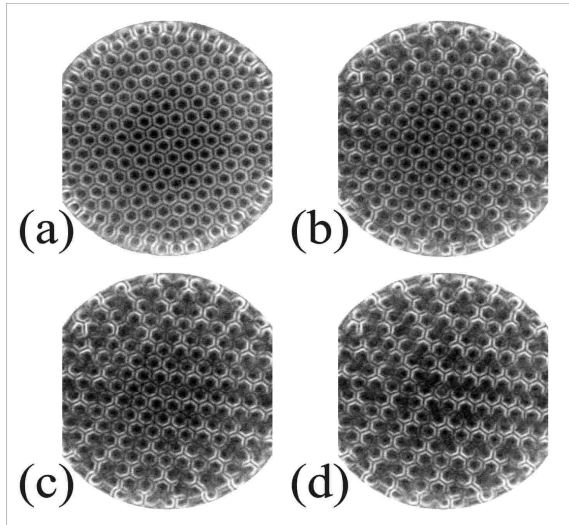


FIG. 8. The transition between Hexagonal and the SSS state is displayed for a typical experiment (40/60). This is a gradual process in which the basic symmetry of a perfect hexagonal pattern (a) is broken first at the circular boundary of the cell. As the amplitude of the external forcing increases, the area of broken symmetry grows inwards (b,c) until the SSS state fills the entire cell (d). This process can also occur in the reverse direction.

Typical time series of the x and y components of the fluid surface gradient at a single point are presented in Figure 9 for three different accelerations. These describe the temporal behavior of hexagons at threshold (a), developed hexagons (b) and SSS-I (c). At threshold, the response is harmonic with respect to the total period of $2\pi/\omega_0$. The response is strongest at the frequency of $\omega_1/2$. Increasing the driving amplitude results in a bifurcation to a state with a strong *superharmonic* response at the frequency of ω_1 . This phenomenon also occurs for single frequency experiments.

A further increase of the driving amplitude yields a second bifurcation. In this bifurcation the temporal response becomes *subharmonic* with respect to the period of $2\pi/\omega_0$. As can be seen in Figure 9 the superharmonic component does not disappear and can be quite strong. It is important to note that $2/n$ driving has some special relations between the various frequencies that are not present for higher order driving (such as $4/5, 4/7, \dots, 6/7, \dots$). For $2/n$ driving $\omega_1/2 = \omega_0$. The temporal response in the harmonic region has the same frequency as the common frequency ω_0 . In other driving ratios, such as $4/5$ driving, the subharmonic is $4\omega_0/2 = 2\omega_0$ where the common frequency is ω_0 . It is possible that such a relation can enhance certain resonant mechanisms and help sta-

bilize certain patterns such as the $2kR$ and oscillon states [19,22].

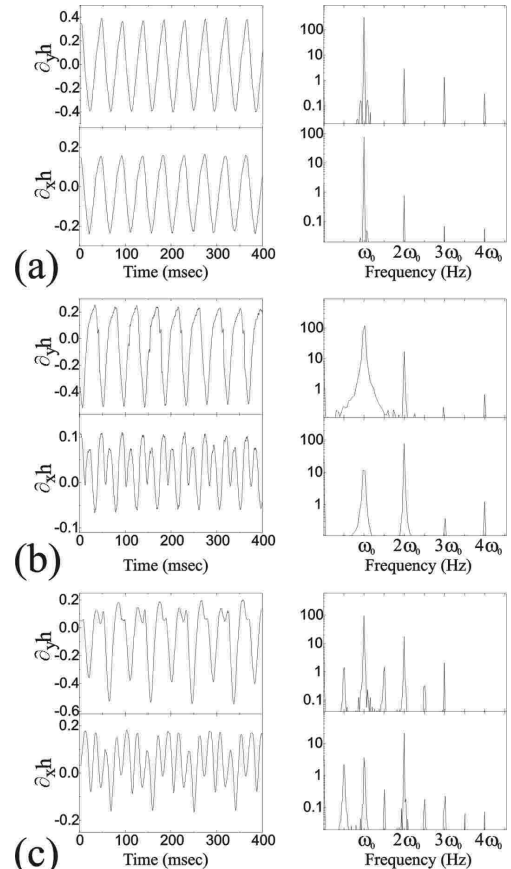


FIG. 9. The time dependence of the SSS-I state as studied by the reflection of a laser by the surface waves. In this experiment, for system parameters $\omega_0/(2\pi) = 22$ Hz, $\nu = 23$ cS, $h = 0.2$ cm, $\phi = 0^\circ$ and $\chi = 36.3^\circ$, increasing the driving amplitude from 2.5 g (a) to 2.9 g (b) and 3.7 g (c) results in (a) Low amplitude hexagons (b) developed hexagons and (c) SSS-I states. In (a) both $\partial_x h$ and $\partial_y h$ have the same peaks in their power spectrum. Increased driving amplitude yields a different temporal response in the two directions x and y . This phenomenon also occurs in single frequency experiments where squares are dominant and may be a general feature of the Faraday instability in viscous fluids. In the SSS-I state (c) a subharmonic temporal response at $\omega_0/2$ occurs.

Wagner et al. [42] studied a two mode system generated by single-frequency excitation at a bicritical point where both harmonic and subharmonic tongues become unstable. They describe two different superlattice states that exist in the transition region between subharmonic squares to harmonic hexagonal states. In the first superlattice state, the square symmetry is broken by a small wavevector \vec{k}_D that is equal to $\vec{k}_H - \vec{k}_S$, where \vec{k}_H , \vec{k}_S are, respectively, the primary hexagonal and square wavevectors. The relative phase of the symmetry breaking \vec{k}_D mode compared to the primary square \vec{k}_S mode can either be 0° or 90° according to the sign of the nonlin-

ear coefficient in the amplitude equation for the symmetry breaking mode. The experimental observation shows that the phase selected for the first transition state is 90° . A second superlattice state [42] was observed that is similar to the SSS-II states found in our experiments. The spatial phase difference, β , between the harmonic hexagonal mode and the subharmonic symmetry-breaking mode was found to be 0° although from amplitude equation considerations 90° is also a possible solution.

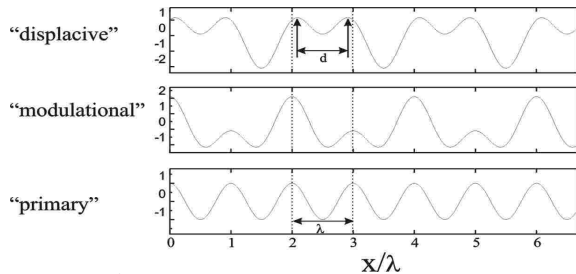


FIG. 10. A simple one-dimensional superposition of a harmonic function (bottom) $\cos(2\pi x/\lambda)$ with its subharmonic can have two basic combinations. The “displacive” mode shown results from the superposition of $\cos(2\pi x/\lambda) + b \cos(\pi x/\lambda + \pi/2)$ (top) ($b = 2.2$ is arbitrarily chosen), whereas a “modulational” mode results from the superposition of $\cos(2\pi x/\lambda) + b \cos(\pi x/\lambda)$ (middle). It can be seen that in the “displacive” mode the distance between local maxima is either d or $2\lambda - d$ with $\lambda - d \ll \lambda$, while in the “modulational” mode the distance between the local maxima remains the same as in the primary mode, λ .

We will now describe in detail the effects of this phase difference on SSS-I states with broken symmetry. Let us first consider the effect of adding a $K/2$ modulation in one dimension. In Figure 10 we can see that adding the $K/2$ mode with $\beta_i = 0^\circ$ results in a modulation of the original cosine form. The waves’ local maxima remain at the same spatial location but their amplitudes are now modulated with a $4\pi/K$ periodicity resulting in one large peak followed by a smaller peak. In contrast to this, adding the $K/2$ mode with $\beta_i = 90^\circ$ results in a different effect. While all of the maxima have the *same* amplitude, their spatial *locations* are modulated with a $4\pi/K$ periodicity. This effect [42] is called “displacive”. The spatial effect in images can be quite pronounced. This is demonstrated in Figure 11 where we present a comparison between the “displacive” (left) and “modulational” (right) effects with spatially subharmonic patterns and symmetry breaking along one direction (top) or three directions (bottom). The effects of symmetry breaking in three directions are more complicated but the qualitative effect remains. We find that SSS-I states are *always* of the displacive nature ($\beta = 90^\circ$). This can be seen by comparing the experimental images shown in Figure 7 with the simulated displacive patterns shown in Figure 11.

It is interesting to note that the “modulational” pattern shown in Figure 11 (bottom right) was seen in an experimental study of the single-frequency Faraday system in a viscoelastic fluid [43]. When changing the driving frequency, Wagner et al. found both a harmonic region for low driving frequencies and a subharmonic response for higher ones. In the vicinity of the transition frequency, Wagner observed a hexagonal superlattice composed of both the subharmonic and harmonic wavevectors. Since the subharmonic wavevector is exactly half of the harmonic one, the simple resonance of $k_S + k_S = k_H$ is retained (where the S index stands for subharmonic and the H for harmonic). Although the power spectra of this superhexagon described by Wagner are similar to the SSS-I power spectra (in the case of three direction symmetry breaking), the real space patterns are different, indicating a 0° spatial phase difference between k_S and k_H , in contrast to the $\beta_i = 90^\circ$ seen for SSS-I.

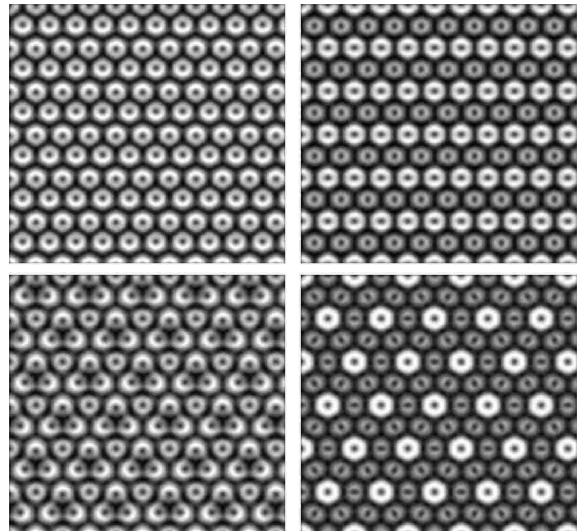


FIG. 11. “Displacive” (left) and “modulational” patterns (right) are shown for both symmetry-breaking in 1 (top) and 3 directions (bottom). The pattern shown is simulated using our imaging model applied to Eq. (3) with $M=1$ ($M=3$) for 1 direction (3 directions) and with $\beta_i = \pi/2$ ($\beta_i = 0$) for the “displacive” (“modulational”) patterns. 2:3 forcing was used with amplitudes of all modes taken to be equal ($A_i = B_i$). All SSS-I patterns were found to be displacive in character (compare to Figure 7).

The combination of the spatial displacive mechanism and the subharmonic temporal dependence of the $K/2$ mode results in an interesting “jittering” effect in time. If we consider Eq. 3 we see that when $t \rightarrow t + 2\pi/\omega_0$ the first part of l.h.s of Eq. 3 is invariant whereas the second part changes sign due to the different time dependence. In our model calculation the temporal displacement of $2\pi/\omega_0$ is equivalent to a spatial displacement of $2\pi/K$ in each of the symmetry-breaking directions. Images photographed at time intervals of $2\pi/\omega_0$ appear to jitter be-

tween these two displaced images, as demonstrated in Figure 12.

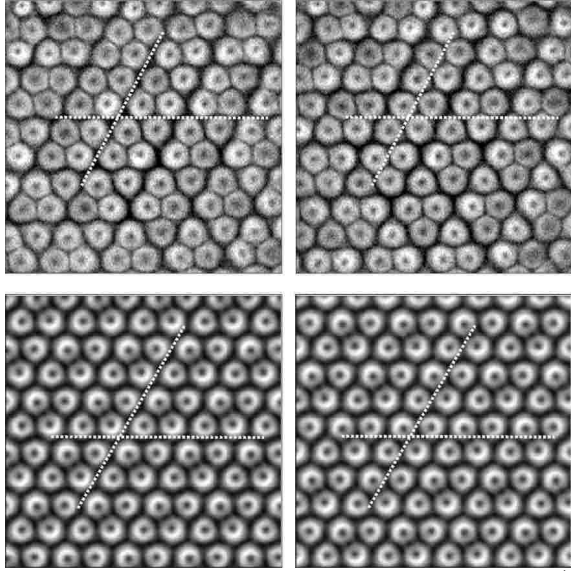


FIG. 12. The “jittering” effect in 2d. Experimental (top) and model (bottom) images of the SSS-I states at two temporal phases separated by a $2\pi/\omega_0$ interval. The white crossed lines are fixed in both frames. The two pictures demonstrate that the time displacement is equivalent to a spatial displacement of $2\pi/K$ in the symmetry-breaking directions.

B. Subharmonic Superlattice type II (SSS-II)

As mentioned above, a qualitatively different type of SSS type pattern, SSS-II, has been observed. Increasing both viscosity and height but keeping the dimensionless parameter δ/h constant (by changing ω_0), results in a different symmetry breaking scenario. Though the SSS-II appears in the same region of phase space as the SSS-I and shares its subharmonic temporal behavior, it is qualitatively different from the SSS-I. The excited vectors \vec{q}_i are now aligned at an angle of $\pi/6$ relative to the vectors \vec{K}_i (in contrast to $\vec{q}_i \parallel \vec{K}_i$ in type SSS-I). The symmetry breaking wavevectors are of magnitude $|q_i| = |K_i|/\sqrt{3}$ and these states exhibit *no* spatial symmetry breaking. For each \vec{K}_i there is a corresponding \vec{q}_i .

Our experiments suggest that SSS-II can be described by:

$$h(r, t) = \cos\left(\frac{1}{2}m\omega_0 t\right) \sum_{i=1}^3 A_i \cos(\vec{K}_i \cdot \vec{r} + \alpha_i) + \cos\left(\frac{1}{4}m\omega_0 t\right) \sum_{i=1}^3 B_i \cos(\vec{q}_i \cdot \vec{r} + \beta_i) \quad (5)$$

$$\vec{K}_1 = K(0, -1); \vec{K}_2 = K\left(\frac{\sqrt{3}}{2}, \frac{-1}{2}\right); \vec{K}_3 = K\left(\frac{-\sqrt{3}}{2}, \frac{-1}{2}\right);$$

and

$$\vec{q}_1 = q(-1, 0); \vec{q}_2 = q\left(\frac{1}{2}, \frac{\sqrt{3}}{2}\right); \vec{q}_3 = q\left(\frac{1}{2}, \frac{-\sqrt{3}}{2}\right); q = \frac{K}{\sqrt{3}}$$

Looking at this state at different temporal phases, the effect of the q_i can be easily seen at some phases (Figure 13a) while, at others, only the hexagonal symmetry is apparent (Figure 13c). This symmetry is a representation of one possible invariant subgroup when hexagonal symmetries are broken [40,41,44].

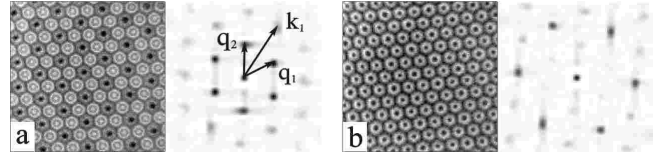


FIG. 13. Images (a,b left) with corresponding power spectra (a,b right) of different temporal phases of an SSS-II state observed for $2/3$ driving in the harmonic region of phase space at $\nu = 47$ cS ($\omega_0/(2\pi) = 25$ Hz and $h = 0.2$ cm). In contrast to the SSS-I pattern, where the primary hexagonal symmetry is broken by wave vectors parallel to \vec{K}_i , SSS-II feature a different symmetry breaking. A second hexagonal lattice of smaller magnitude wave vectors forms, obeying the resonance condition $\vec{q}_1 + \vec{q}_2 = \vec{K}$. At certain temporal phases the effect can be easily seen (a) while at others only the hexagonal symmetry is dominant (b).

In the $1/2$ driving experiments performed by Muller [12] a transition between hexagonal and triangle patterns was observed that corresponds to a change of $\sum_i \alpha_i$ in Eq. (5) from the value of 0 to $3\pi/2$ (where the second term of the R.H.S. of Eq. (5) is zero). A similar phenomenon can take place with SSS-II states. As shown in Figure 14, a variant of the SSS-II states occurs with a rotational symmetry of $2\pi/3$ in contrast to the $2\pi/6$ that is typical for hexagon patterns. These SSS-II variants are observed for $2/3$ driving when relatively higher frequencies ($\omega_0 > 40$ Hz) are used. Using our imaging model, we find that these patterns are formed by the same resonance as the SSS-II but when spatial phase angles of the \vec{q}_i modes are $\beta_i = \pi/2$ for $i = 1, 2, 3$ or $\sum_i \beta_i = 3\pi/2$. These SSS-II states have symmetries that are similar to those of the time-averaged symmetries and wavenumbers of the “SL2” states observed in [21]. The instantaneous images of SL2 states, however, are more reminiscent of SSS-I states (as shown in Figure 6). Patterns similar to this SSS-II variant have recently been observed in a forced ferrofluid system [45] in the vicinity of a bicritical point where harmonic and subharmonic solutions collide. Muller shows that when considering a harmonic region amplitude equation with quadratic terms for a single wavenumber model, only solutions where $\sum_i \beta_i = 0$ are possible. It appears that the second set of equations for the q wavenumber modes, which are temporally *subharmonic*, does allow the exis-

tence of modes with $\sum_i \beta_i = 3\pi/2$ solutions. The mechanism that selects the spatial phase in multi-mode systems still must be clarified.

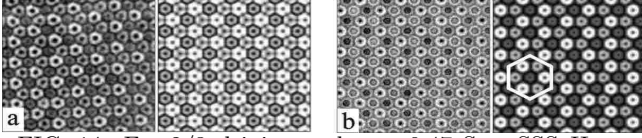


FIG. 14. For 2/3 driving and $\nu = 0.47\text{cS}$, a SSS-II type pattern with a different spatial dependence occurs. Two phases of this state are shown in (a,b left) and a simulation of these pattern are shown in (a,b right). These patterns are formed when the spatial phases of the smaller wavevectors, (\vec{q}_i) , are shifted by $\pi/2$ relative to \vec{K}_i . These states were observed for higher frequencies ($\omega_0 > 35$ Hz) than those for which SSS-II having a zero phase shift are observed.

SSS-II type patterns have also been observed in the experimental study of optical pattern formation in sodium vapor [46]. In the next section we will address the question of a selection criterion between the SSS-I and SSS-II states.

C. Selection between SSS-I and SSS-II

Both SSS-I and SSS-II break the temporal symmetry of the initial hexagon state by temporal period-doubling to a basic frequency of $m\omega_0/4$. The two states, however, differ in their spatial behavior. For the case of SSS-I states, the excited wavevectors, \vec{q}_i , are both parallel to the linearly unstable wavevectors \vec{K}_i , and, in many cases $q = K/2$. In contrast, the excited wavevectors in SSS-II states are rotated by $\pi/6$ relative to \vec{K}_i . What mechanism governs the selection of both the two different states and the values of q that are excited?

As Silber, Topaz and Skeldon have suggested [33], the symmetry-breaking wavevectors of harmonic patterns may correspond to minima of linearly stable tongues that can be excited via nonlinear coupling to the \vec{K}_i modes. Since the subharmonic frequency, $m\omega_0/4$, is excited by all of the SSS states, the linearly stable tongue with a dominant $m\omega_0/4$ frequency would be a likely candidate to be selected. The wavenumber, q , corresponding to these waves, can be well-approximated by the linear dispersion relation $q = k(m\omega_0/4)$. Note that q is not constant for a given value of ω_0 , but can be strongly dependent on the parameters ν and h .

Let us now examine the following premise. The system will generically prefer to undergo spatial period doubling to $q = K/2$. If, however, $\vec{q}(m\omega_0/4)$ is close to a wavevector \vec{q} with a magnitude that is substantially different than $K/2$, one possible solution of the system is to lock to either SSS-I or SSS-II patterns with $q \neq K/2$. If q is near $K/\sqrt{3}$, the system will lock to this value, thereby fulfill-

ing the spatial resonance condition: $\vec{q}_i + \vec{q}_j = \vec{K}_i$. SSS-II patterns will then occur. Values of q sufficiently far from either spatial resonance will result in an SSS-I state with $q \neq K/2$. Such a state is presented in Figure 15 where symmetry breaking occurs in either one direction (Figure 15a,b) or three (Figure 15c) but the symmetry-breaking wavevector's magnitude was *not* $K/2$. Instead, vectors parallel to \vec{K}_i , with magnitudes $q \neq K/2$ and $K - q$ are observed, with, empirically, $q \sim 0.6k_c$.

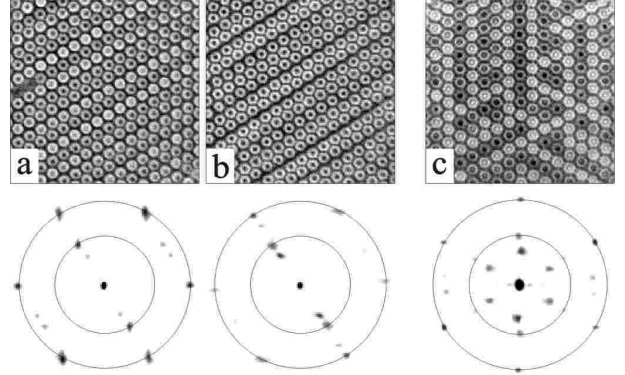


FIG. 15. Images (top) and corresponding power spectra (bottom) of SSS-I superlattices observed for 2/3 driving in which $q \neq K/2$. Circles of a radii K (outer) and q , corresponding to the $m\omega_0/4$ frequency (inner) are drawn. The primary hexagonal symmetry is broken either in one direction (a,b) or in three directions (c). (a,b) show the same state at different temporal phases. The relative intensities of \vec{q} and $\vec{K} - \vec{q}$ vary in the different phases. All experiments were with $\nu = 23$ cS. (a,b) for $h = 0.2$ cm and (c) for $h = 0.25$ cm. The basic frequency was $\omega_0/(2\pi) = 35$ Hz for (a,b) and $\omega_0/(2\pi) = 30$ Hz for (c). The value of q/K is ≈ 0.6 for all experiments.

This premise is checked in Figure 16, where we plot the value of the ratio between the experimentally measured values of q and the wavenumber computed for single frequency driving using $m\omega_0/4$ with K for parameters where different SSS-type patterns were observed. The plot shows that for both SSS-II and the SSS-I with $q \neq K/2$ the approximation $q = k(m\omega_0/4)$ is correct to within 4%. In SSS-I states where $q = K/2$ is the symmetry breaking mode, the ratio $q/k(m\omega_0/4)$ varies *systematically* between 77% – 85%. This suggests that the $\vec{q} = \vec{K}/2$ resonance is strong enough to induce this “locking” or detuning of q .

For 2/3 driving we observed the appearance of SSS-I states at lower liquid layer depth and the SSS-II at higher depths. As h is reduced, we found that instead of an abrupt transition between the SSS-I and SSS-II states, both types of symmetry breaking can occur *simultaneously*. As shown in Figure 17, the primary hexagonal symmetry of this state is broken by two 6-fold sets of wavevectors.

One set corresponds to SSS-I with magnitude $q_0 =$

$K/2$ while the other set corresponds to SSS–II, with $q_1 = K/\sqrt{3}$. In real space the characteristic pattern of SSS–II (Figure 17b) is broken by superimposed stripes in one direction. This state has both modulative and displicative effects implying that the two symmetry–breaking modes retain their respective spatial phase characteristics.

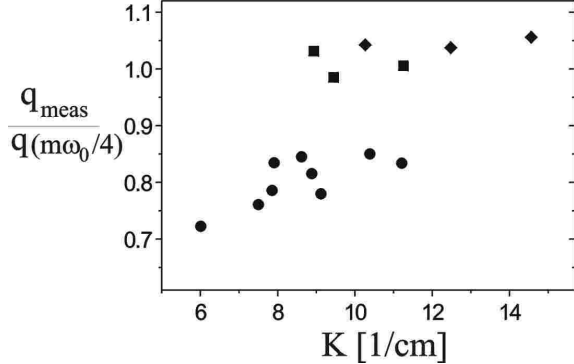


FIG. 16. The measured wavenumber, q_{meas} , of the symmetry breaking wavevectors in SSS–type patterns, normalized by the linear wavenumber calculated for the frequency $m\omega_0/4$ as a function of the measured critical wavenumber of the primary hexagon pattern, K . The symbols correspond to different types of SSS patterns; SSS–I patterns with $q = K/2$ (circles), SSS–I with $q \neq K/2$ (diamonds) and SSS–II patterns with $q = K/\sqrt{3}$ (squares). The data indicate that the first type of pattern ($q = K/2$) is generally preferred by the system unless the value of $q(m\omega_0/4)$ is either close to $q = K/\sqrt{3}$ or sufficiently far from either of these preferred modes.

As demonstrated in Figure 16, the mechanism that forms both the SSS–I and the SSS–II patterns depends on a “slaved” linear eigenmode. In the $2/3$ driving described above the only existent linearly stable subharmonic tongue occurs for $\omega_0/2 = m\omega_0/4$. In contrast to $2/3$ driving, even/odd driving ratios with m/n values such as $4/5$, $6/7$ etc. possess linearly stable tongues whose dominant frequencies differ from $m\omega_0/4$. For example, in $60/75$ Hz driving, besides the 15 Hz ($= m\omega_0/4$) response observed for the SSS state, a response at 7.5 Hz ($= \omega_0/2$) is also possible. Recent theoretical work by Silber et al. [33] has suggested that these additional slaved modes can influence the character of the selected nonlinear state. We find that these additional slaved modes can indeed appear. In $4/5$ driving typical SSS–I states with a frequency response of $m\omega_0/4$ are observed far from χ_c . Near χ_c , both the 12 –fold temporally harmonic quasicrystalline states first described by Edwards and Fauve [18], as well as a state composed of a *cascade* of symmetry-breaking bifurcations occur. This second type of pattern, which has a subharmonic time dependence, is shown in Figure 18a.

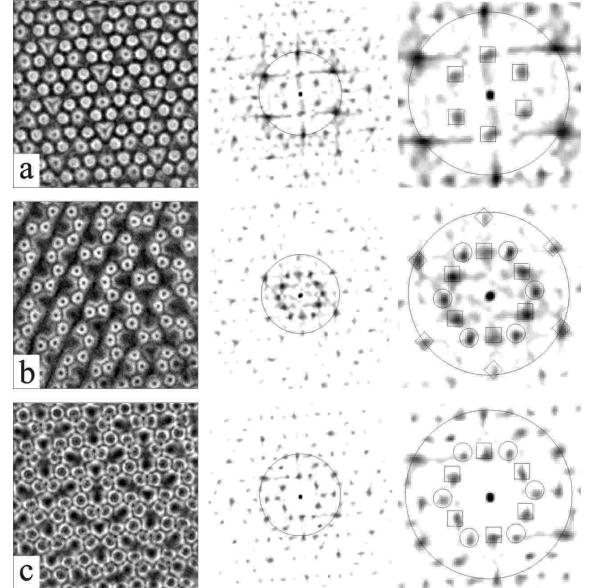


FIG. 17. Reducing h from $h = 0.33$ cm where only SSS–II was observed to $h = 0.31$ cm results in a state where the two types of SSS patterns SSS–I and SSS–II can coexist. In (a–c) the combined state images (left), full power spectra (middle), and expanded power spectra (right) are presented at different temporal phases. The primary hexagonal symmetry (of magnitude \vec{k}_o) is broken by two different sets of wave vectors arranged in two 6–fold sublattices. The set corresponding to the SSS–I is enclosed in squares. The set corresponding to the SSS–II is enclosed in circles. This state was observed for $2/3$ driving and system parameters of $\nu = 47$ cS, $\omega_0/(2\pi) = 25$ Hz and $h = 0.31$ cm, $\chi = 62.5^\circ$ and $\phi = 0^\circ$.

This “cascaded” state appears as either a secondary bifurcation of an initial hexagon pattern or as a bifurcation from a 12 –fold quasipattern state. In its spatial power spectrum the two mechanisms that appeared in both SSS–I and SSS–II type patterns are cascaded and appear at different scales. An SSS–II type resonance occurs where wavevectors \vec{q}_i with magnitudes $q_i = K/\sqrt{3}$ appear. A *third* vector \vec{Q} , however, is also present. \vec{Q} is half the magnitude of \vec{q}_i and, echoing the mechanism forming SSS–I states, breaks the 6 –fold symmetry of the \vec{q}_i by aligning itself parallel to a single vector, \vec{q} .

Figure 18b demonstrates that this state has an overall temporal periodicity of $2\pi/\omega_0$. The two images (b left, right) were taken at an interval of π/ω_0 . The images look exactly the same but with a transverse displacement of the $d = 4\pi/K$ length scale. The symmetry breaking by the \vec{Q} is similar to the SSS–I mechanism where a mode with a phase of $\pi/2$ produces a displicative effect, as shown in Figure 18b. The peaks are of high amplitude and have the characteristic shape of the oscillons described by Arbell and Fineberg [19] modified by the asymmetry that is produced by the displicative effect of the \vec{Q} mode.

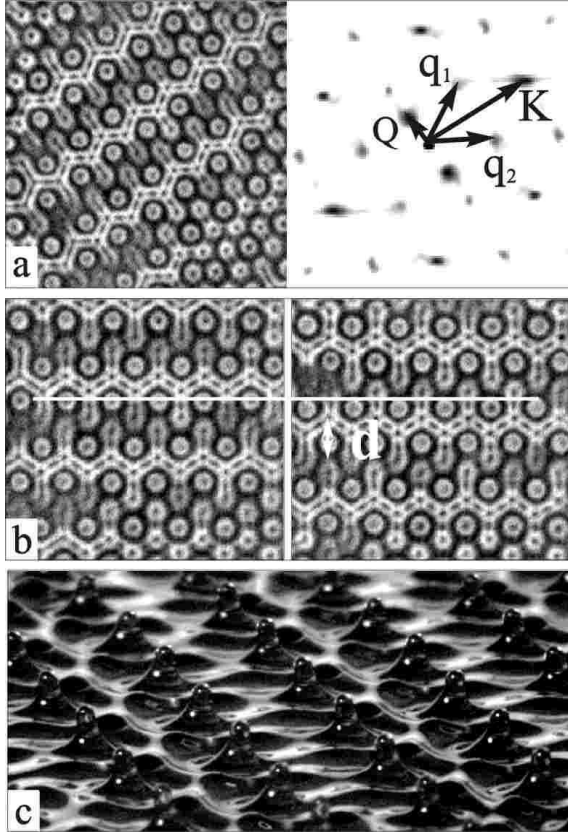


FIG. 18. (a) The image (left) and power spectrum (right) of “cascaded” SSS states appearing for $4/5$ driving near χ_c . The two mechanisms appearing in SSS-I and SSS-II coexist at different scales. A hexagonal sublattice of $q_i = K/\sqrt{3}$ bifurcates from the original hexagonal pattern. In addition, a *third* wavevector $\vec{Q} \neq \vec{q}$ breaks the symmetry of this sublattice in a single direction. This state has an overall temporal periodicity of $2\pi/\omega_0$. This is demonstrated in (b) where two images (b left, right) were taken at an interval of π/ω_0 . The images are displaced by a $d = 4\pi/K$ length scale. The horizontal white line indicates the location of the peaks in the first phase (b left). (c) A the side view of this state. The peaks are of high amplitude and have the characteristic shape of the oscillons described by Arbell and Fineberg [19] with a small asymmetry in the direction of \vec{Q} . These images were observed for system parameters of 75/60 Hz, $\nu = 23$ cS, $h = 0.2$ cm, $\chi = 56^\circ$ and $\phi = 0^\circ$.

As demonstrated by Figure 19, different wavevectors are dominant at different temporal phases. These states were not observed in experiments with higher m/n values such as $6/7$ and $8/9$ driving ratio.

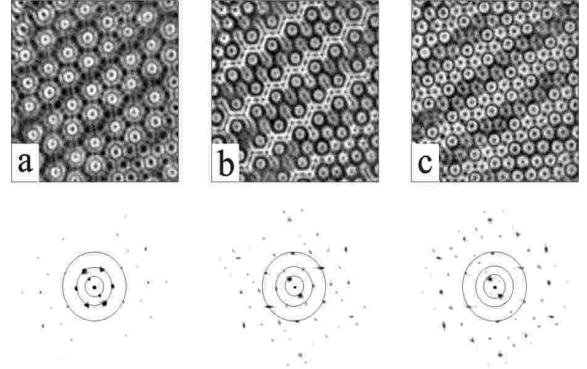


FIG. 19. Images (a-c top) and the corresponding power spectrum (a-c bottom) of different temporal phases of the SSS type pattern shown in Figure 18 that appears in $4/5$ driving experiment. The original hexagonal wave vector is drawn as the outer circle in the power spectrum shown (a,b bottom). It can be seen that the different wave vectors have different relative amplitudes at different temporal phases. In (a) the two smaller wave vectors \vec{Q} and \vec{q} have higher intensities than the wavevector \vec{K} along the outer circle, where in (c) the center circle of radius q has a very small intensity.

V. DOUBLE HEXAGON SUPERLATTICES (DHS)

Historically, the first two-frequency experiment focused on quasicrystalline patterns with 12-fold symmetry. These were observed in the vicinity of χ_c in systems driven with an even/odd driving ratio and were found to bifurcate either from the flat state or as a second bifurcation from the harmonic hexagon region. In this section we will describe both the 12-fold quasipatterns mentioned above and two other superlattice states (see Figure 20). All of these states share a harmonic temporal response for odd/even driving and appear in the same general area of phase space. An important factor in pattern selection is the nonlinear coupling coefficient that depends strongly on resonant locking (see Sec. ID 2). In contrast to the SSS states, we will see below that no *new* wavenumbers are needed to construct these states. This class of superlattice patterns are differentiated by both the relative angular orientation and spatial phase relations of the critical wavevectors that form them.

The 12-fold quasipattern (see Figure 20a) was observed for $4/5$ driving in the vicinity of χ_c . This state’s temporal behavior is harmonic with respect to ω_0 . This state can be formed near the linear threshold for small values of $\epsilon \sim 0.01$. Increasing the amplitude A causes a bifurcation to the cascaded-type superlattice described in IVC (see Figure 18). The 12-fold quasipattern may also be understood as being formed by two sets of hexagonal wavevector at 30° to each other. As in all quasicrystals, this state does *not* have long range order or a well defined sub-unit cell. It is interesting to note that unlike the quasipattern described in [17] that appeared only for

$\phi \sim 75^\circ$ the quasipattern we describe exists for $\phi = 0^\circ$.

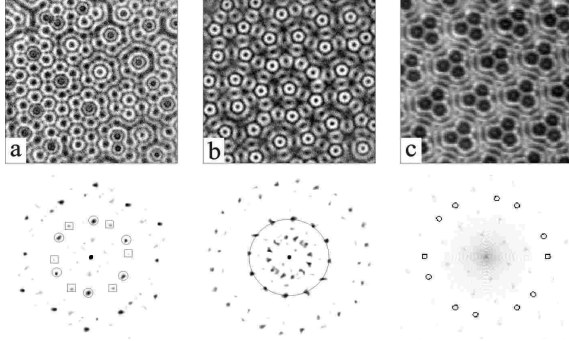


FIG. 20. When using even/odd driving, a class of temporally harmonic states exists that is composed of two distinct hexagonal sublattices (delineated by squares and circles) of size K , the critical wavenumber of the harmonic driving component. (a) Double Hexagon State (DHS) formed by both the critical hexagonal lattice and an additional hexagonal sublattice of smaller amplitude which is rotated by an angle of $\sim 22^\circ$. (b) 12-fold quasicrystalline state (c) A similar (“SL1”) state observed by Kudrolli et al. [21] for 6/7 driving. This state is formed by a resonance similar to (a) but with spatial phase of $2\pi/3$ in each of the sublattice components. (a) and (b) were obtained for 4/5 (60/75 Hz) forcing. (c) was reproduced with permission from [21].

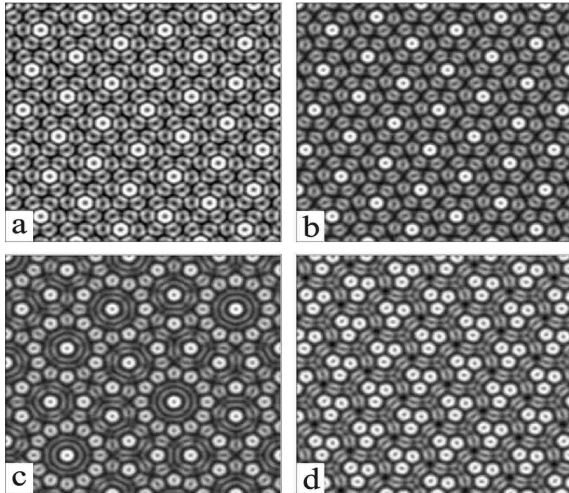


FIG. 21. Using our numerical modelling technique, we calculated the images of a perfect double hexagon state (DHS) formed by two hexagonal lattices rotated by 22° . (a) $\alpha_i = \beta_i = 0$ (see Eq. (6)) shows a negative crater state and (b) a positive peak state. (c) shows the calculated image of a 12-fold quasi-pattern. (d) A calculated DHS state with spatial phases of $\alpha_i = 0$ and $\beta_i = 2\pi/3$ as in Figure 20(c).

Another superlattice pattern (Figure 20c) which occurs in this regime of phase space was first studied by Kudrolli et al. with 6/7 driving ratio with $\omega_0/(2\pi) = 16.44Hz$, $\nu = 20CSt$, and $h = 0.3cm$. They found a hexagonal superlattice pattern composed of two hexagonal sets of critical wavevectors with harmonic temporal response. The

equation that describes the surface height function of this pattern can be generally written down as:

$$h(r) = \sum_{i=1}^3 A_i \cos(\vec{K}_i \cdot \vec{r} + \alpha_i) + \sum_{i=1}^3 B_i \cos(\vec{K}'_i \cdot \vec{r} + \beta_i), \quad (6)$$

where $|K| = |K'| = k_c$ and

$$\vec{K}_1 = K(1, 0); \vec{K}_2 = K(-\frac{1}{2}, \frac{\sqrt{3}}{2}); \vec{K}_3 = K(-\frac{1}{2}, -\frac{\sqrt{3}}{2});$$

and \vec{K}'_i can be obtained by rotating \vec{K}_i by an angle of $\theta = 22^\circ$. In Figure 21a,b,d we show simulated images of this equation for different values of β and A_i/B_i .

The pattern (Figure 20c) described by Kudrolli et al. was found to have an angle θ with the value $\theta = 2 \sin^{-1}(1/2\sqrt{7}) \approx 22^\circ$, equal amplitude coefficients $|A_i| = |B_i|$ for $i = 1, 2, 3$ and spatial phase angles $\alpha_i = 0^\circ$ and $\beta_i = 120^\circ$. For this special value of θ , resonance conditions such as $2\vec{K}'_1 - \vec{K}'_3 = 2\vec{K}_1 - \vec{K}_3$ were shown [21] to exist.

Double hexagon states formed by the superposition of two hexagon sets of critical wavevectors oriented at a relative angle $\theta = 2 \sin^{-1}(1/2\sqrt{7})$ are one example [23,40] of a wider class of superlattices. This superlattice class is composed of a periodic lattice formed by a wavenumber smaller than the critical wavenumber of the excited surface waves. This smaller wavenumber corresponds to the six wavevectors formed by the difference between adjacent wavevectors of the two hexagonal sets i.e. by $\vec{Q}_i = \vec{K}_i - \vec{K}'_i$ for $i = 1, 2, \dots, 6$. Any two of these wavevectors, say \vec{Q}_1 and \vec{Q}_2 , are primitive vectors of the lattice and the vectors \vec{K}_i and \vec{K}'_i are points on the Q -lattice given by $\vec{K}_i = n_1\vec{Q}_1 + n_2\vec{Q}_2$. Silber and Proctor [23] show that only a discrete countable set of \vec{Q}_i where $K/Q = \sqrt{n_1^2 + n_2^2 - n_1n_2}$ can satisfy this condition. The angle θ between the two lattices is given by $\theta = \cos^{-1}(\frac{n_1^2 + 2n_1n_2 - 2n_2^2}{2(n_1^2 - n_1n_2 + n_2^2)})$. In this formulation the experimentally observed patterns are obtained for $n_1 = 3$, $n_2 = 2$ and $K/Q = \sqrt{7}$, giving $\theta \approx 22^\circ$. Only the simplest DHS have been observed to date.

One characteristic aspect of the DHS states is the relative spatial phase of the different wavevectors. The pattern described by Kudrolli et al. [21] (coined “SL-1”, see Figure 20c) consisted of triangular unit cells that were produced by a DHS with $\alpha_i = 0^\circ$ and $\beta_i = 120^\circ$. Silber and Proctor describe, in simulations of thermal convection, a DHS state formed with both $\alpha_i = 0^\circ$ and $\beta_i = 0^\circ$ [23]. The DHS superlattice in our experiments with a 2/3 driving ratio (see Figure 20a) differs from these superlattices in that the two hexagonal sublattices that form them possess *different* amplitudes. States similar to these have been observed in nonlinear optics [47]. In addition, in our

case, there is no spatial phase difference between the two sets of hexagonal wavevectors ($\alpha_i = \beta_j$ for all i, j).

Although this state is stable close to the threshold, increasing the driving amplitude results in the appearance of many defects and eventual temporal disorder. At high driving amplitudes the spatial symmetry is hard to discern due to the many defects and domains within the fluid cell. In Figure 22 we show a typical DHS state at different temporal phases. The state oscillates between a crater-like phase (a) and a positive oscillon-like phase with a frequency of ω_0 . High amplitude oscillons appear in the center of the hexagonal sub-unit cell of the DHS state. Similar oscillons were also observed for the 12-fold quasipattern state shown in Figure 20b [19].

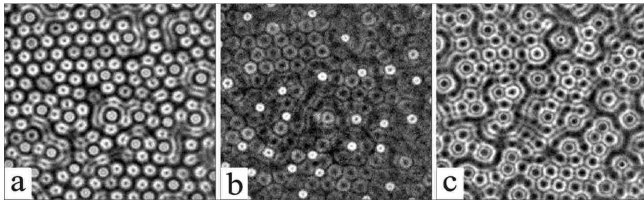


FIG. 22. Typical images of the double hexagon state (DHS) taken at different temporal phases. (a) shows a crater phase (b) an intermediate phase and (c) a peak phase for $2/3$ driving with $\omega_0 = 30$ Hz, $h = 1.55$ cm, $\nu = 23$ cS and $\chi = 60.4^\circ$. The time interval between (a) and (b) is $0.25T$ and between (a) to (c) is $(0.4T)$

Let us summarize the common characteristics of DHS states. All of the patterns reveal a harmonic time dependence and the lack of any *fundamental* wavevectors other than the critical wavevectors excited by the harmonic frequency. All of these patterns were observed to be in the vicinity of χ_c on the harmonic side. In all cases, the mixing angle was greater than that needed for obtaining SSS states and within the range $\chi_c^\circ > \chi > (\chi_c - 12^\circ)$. Another common characteristic of these states is that all exist in the vicinity of a first-order transition of the hexagonal patterns from the featureless fluid state. This implies that quadratic interactions can play an important part in describing these states. Finally, two of these patterns also generate oscillons as described in detail in [19].

VI. TWO MODE SUPERLATTICES (2MS)

In the vicinity of the critical mixing angle, χ_c , two modes with different wavelengths can be excited concurrently. These modes can interact in different ways to produce a variety of different patterns. In the next two sections we will describe two distinct types of two-mode states that are formed near χ_c . The first of these states are two-mode superlattices (2MS). These states are formed by the interaction of the two linearly excited modes with a third “slaved” mode that is selected via a

temporal resonance.

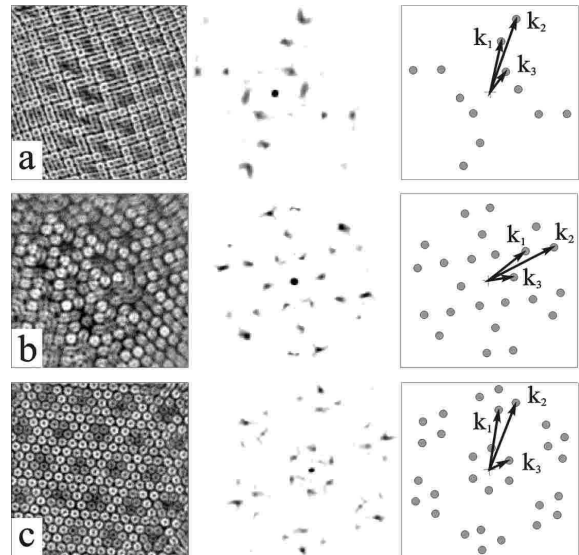


FIG. 23. 2MS patterns consist of a nonlinear superposition of *both* eigenmodes, k_1 and k_2 , excited by the driving frequencies ω_1 and ω_2 . Although ω_1 and ω_2 determine the lengths of k_1 and k_2 , their relative orientations are determined by the condition: $\vec{k}_3 = \vec{k}_2 - \vec{k}_1$ where the wavenumber, k_3 , is determined by the temporal resonance condition: $\omega_3 = \omega_2 - \omega_1$. (a) 2MS patterns for 50/80 Hz driving where k_2 with square symmetry is dominant. (b) k_2 -dominant 2MS with hexagonal symmetry for 45/60 Hz driving and (c) k_1 -dominant states having hexagonal symmetry for 40/60 Hz. Shown are the spatial spectra (center) with the resonant triads (right) $\vec{k}_3 = \vec{k}_2 - \vec{k}_1$, highlighted.

Figure 23 shows the three main types of 2MS states; k_2 dominated (with either square or hexagonal symmetries) and k_1 dominated (with hexagonal symmetry). 2MS states exist in both harmonic and subharmonic regions of phase space in the vicinity of χ_c (see Figure 4). In the region of phase space between the square 2MS and the hexagonal 2MS a spatially disordered “unlocked” state exists. Unlocked states, which are formed by the same wavenumbers that form the 2MS, have no well-defined spatial symmetries. As in the case of SSS states, the transition to 2MS from either square or flat states is non-hysteretic and occurs via propagating fronts.

The 2MS are qualitatively different than SSS states. They result from spatial phase locking of *both* k_1 and k_2 whereas the SSS states result from a resonance condition that is *independent* of the k_2 mode. 2MS states are the most general of the superlattice states described here. They are observed for all types of driving parities (odd/even, even/odd and odd/odd) and, as shown in Figure 23, appear with either square or hexagonal symmetry.

A. 2MS Resonance condition

2MS spatial spectra, as shown in Figure 23, are composed of peaks of length k_1 and k_2 and their linear combinations. The strongest secondary peaks, indicated in the figure, are given by $\vec{k}_3 = \vec{k}_2 - \vec{k}_1$ where the magnitude of k_3 is consistent with the linear value of k calculated for a single frequency excitation at the difference frequency $\omega_3 = \omega_2 - \omega_1$. Our calculated value of k_3 was obtained using the *linear* single frequency code of [14] at threshold. The difference between the calculated and measured values of k_3 varies between 5 – 20%. This shift between the measured and calculated values is constant for a given value of the difference frequency, ω_3 , and systematically decreases as ω_3 increases. We believe the shift to be the result either finite size effects in the cell or the fact that the $\omega(k)$ used is the linear dispersion relation for a *featureless* state (not one with pre-existing waves).

A subtle point in the interpretation of the power spectra of 2MS states, is the evaluation of the magnitude of the two wavevectors that appear. As can be seen in Figure 24 the values of k_1 and k_2 measured in the vicinity of χ_c are significantly different than the values of k excited by single frequency excitation. The two-frequency linear stability code of Tuckerman [13,35], reproduces this effect and agrees to within 1 – 2% with the experimentally measured values (see Figure 24). This enables us to accurately calculate values of both k_1 and k_2 in the vicinity of χ_c .

The resonant conditions stated above suggest that the orientation of the wavevectors building the 2MS is selected by nonlinear interactions that are resonant both in space and time. Thus, the temporal resonance condition dictates the spatial orientation of the vectors \vec{k}_1 and \vec{k}_2 . Such 3-wave resonant interactions have been predicted to occur in non-linear interactions of surface waves [48] and are well known in the physics of plasmas. Similar states were observed as a result of nonlinear mixing of a multiple-mode optical beam [49]. The selection of k_3 via the temporal resonance condition yielding ω_3 is non-trivial and can not be accounted for by experimental artifacts such as possible nonlinearities in the imaging. This 3-wave resonance condition occurred for *all* frequency ratios tested.

As in SSS, the dominant 2MS wavevector retains its initial symmetry, while the relative orientation of the other linearly excited wavevectors are determined by the above resonance condition. For odd/even driving hexagonal (square) symmetry dominates for $\chi < \chi_c$ ($\chi > \chi_c$). Thus, square 2MS (Figure 23a) bifurcate from the k_2 square pattern that dominates the $\chi > \chi_c$ region. Similarly, hexagonal 2MS (Figure 23b) bifurcate from the k_1 hexagonal pattern that dominates the $\chi < \chi_c$ region. In 3/4 driving, hexagonal 2MS states are excited whose dominant scale is that of the larger wavenumber, k_2 (Fig-

ure 23c). It is known that in single-frequency driving experiments different symmetries can arise for different system parameters even when the temporal behavior is solely subharmonic. In two-frequency driving experiments the parity of the dominant frequency does not automatically dictate the symmetry selected. For example, in 5/8 driving (50/80 Hz) 2MS states are observed with square symmetry in the temporally *harmonic* region.

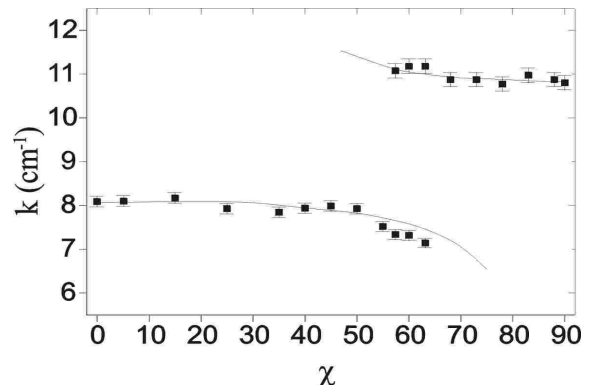


FIG. 24. A comparison of k (in cm^{-1}), calculated using the two-frequency linear calculation [13] (solid line), with measured values of k as a function of χ . Note that both values of k are nearly constant away from $\chi_c = 58^\circ$. Near χ_c , k_1 (corresponding to $\omega_1 = 40$ Hz) decreases by nearly 10% while k_2 (corresponding to $\omega_2 = 60$ Hz) increases slightly.

B. Temporal behavior of 2MS

Using our strobed imaging technique, we studied the spatio-temporal behavior of the patterns by inspecting them at different temporal phases. The 2MS inherit the basic temporal periodicity of *both* primary eigenfunctions, which are periodic in time with a basic frequency of either ω_0 (harmonic) or $\omega_0/2$ (subharmonic). The superposition of the two modes always displays a subharmonic response ($\omega_0/2$). Like the SSS, the state's appearance changes qualitatively with time, with the spatial wavenumbers having fixed *locations*. 2MS time-dependence stems from the temporal dependence of the *amplitudes* of these modes. In Figure 25 and Figure 26 we see typical sequences of both square and hexagonal 2MS states taken at constant values of the driving parameters. The relative intensities of the different wavevectors change in the different phases; in Figure 25e the k_1 and k_3 wavevectors are almost absent, resulting in a pattern whose dominant square symmetry has a $2\pi/k_2$ scale, while in the remainder of the phases all vectors appear. In Figure 26 the resonance condition allows k_1 and k_2 to be nearly co-linear and two sets of 6-fold wavevectors appear in the power spectrum. As in the square 2MS, one can see phases with significantly stronger k_1 peaks (Figure 26(a)) as well as those where either the k_3 (Figure

26(b)) or k_2 (Figure 26(c)) are stronger.

The relative stability of 2MS hexagonal states (e.g. Figure 23b,c) is dependent on whether k_1 or k_2 is dominant. Let us first consider hexagonal 2MS states where k_1 dominates. This state is found for even/odd driving for $\chi < \chi_c$ (see Figure 4) and a typical time sequence is presented in Figure 27. Again, different wavenumbers are dominant in different temporal phases.

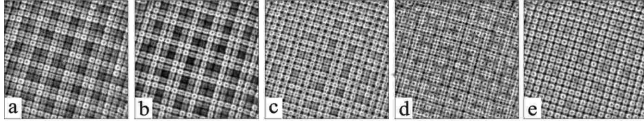


FIG. 25. A typical temporal sequence of square 2MS states taken at constant parameter values for 50/70 Hz driving. k_1 (middle circle), k_2 (outer circle) and k_3 (inner circle) are indicated in (a). In (d) the k_3 vectors are absent but enclosed in squares are vectors that are the vector sum $\vec{k}_3 + \vec{k}_3$. System parameters are $\omega_0/(2\pi) = 20$ Hz, $\nu = 23$ cS, $\phi = 0^\circ$, $\chi = 65.4^\circ$, and $h = 0.155$ cm.

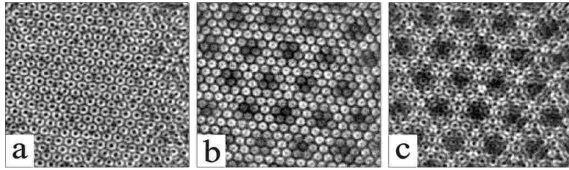


FIG. 26. A typical sequence of *hexagonal* 2MS (a-e) at different temporal phases taken at constant parameter values for 60/80 Hz driving. Circles of radii k_1 (middle), k_2 (outer) and k_3 (inner) are drawn in (c). In (b) the k_3 and k_1 vectors interact to produce the vectors enclosed squares. k_1 and k_2 form two sets of hexagonally arranged vectors.

The region of phase space where this state appears is not as large as the k_2 dominant 2MS, but these states appear for all even/odd driving ratios used. As in the case of square 2MS and the $2kR$ states discussed in Section VII, these states are not observed for all combinations of ϕ and δ/h used. It is difficult to obtain a hexagonal 2MS state of this kind that extends over the entire system and k_1 -dominant hexagonal 2MS states generally occur within domains. Thus the spatial spectra (as seen in Figure 27) appears sometimes smeared, as the various domains have different angular orientations. Although

the scenario described in Figure 27 is typical, we have observed stable global k_1 -dominated 2MS state for particular values of ϕ and δ/h (see e.g. Figure 52).

A typical time sequence and power spectra for the k_2 dominant hexagonal 2MS state (shown in Figure 23c) is presented in Figure 26. Here, in contrast to k_1 dominant hexagonal 2MS, the pattern is global with a well-defined symmetry in all of its temporal phases. Hexagonal symmetry was *not* seen to be preferred for all odd/even driving and was only observed for the simple ratios of 1/2 and 3/4. This might be a feature of simple driving ratios that can sometimes have unique properties which are related to temporal locking ([11,33]).

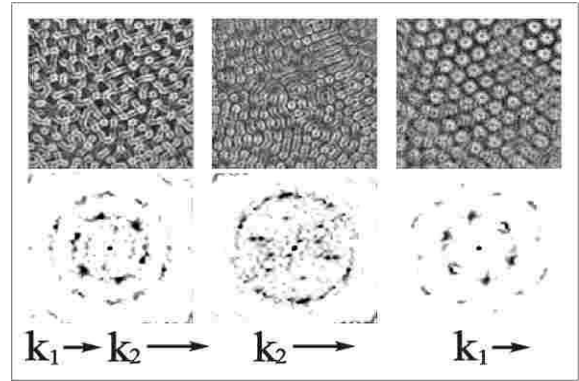


FIG. 27. A typical sequence of k_1 -dominant hexagonal 2MS states taken at constant parameter values for 40/70 Hz driving. These states generally appear in domains. (Wavenumbers are noted by arrows).

2MS states are not always as highly ordered as those in Figure 25 and Figure 26. When highly ordered 2MS states occur, the resonance condition for these parameters allows k_1 , k_2 and k_3 to be nearly co-linear. When the angles between the resonant wavevectors are not small the pattern is usually not global and a number of domains coexist. In highly ordered states we find a locking of the wavevectors' magnitude to small natural number ratios. The locking ratios of $k_1 : k_2 : k_3 = 1 : 3 : 4$ and $1:4:5$ were, respectively, obtained in Figure 25 and Figure 26. This “spatial locking” seems to stabilize global patterns in a way similar to the global SSS states presented in Section III.

The local laser probe technique provides more detailed, quantitative, information of the temporal behavior of 2MS states. In Figure 28 we show one component of the slope of surface waves obtained for 4/5 driving. In Figure 28(a) we show the typical waveform of a hexagonal pattern for $\chi < \chi_c$. Besides the strong component at $\omega_1/2 = 4\omega_0/2$ and its harmonics (40,60,80 Hz ...), peaks appear at values of $j\omega_0, j = 1, 2, \dots$. Those peaks are expected from the linear theory. In Figure 28(b) we see a typical waveform of a square pattern for $\chi > \chi_c$. Although the strongest frequency response is at $\omega_2/2$,

the basic frequency, $\omega_0/2$, together with its higher harmonics also appear. Linear theory predicts a different distribution of energy in the peaks for the unstable mode at threshold. Zhang and Vinals [11] non-linear theory accounts for the peak's strength in a semi-quantitative way, as it correctly predicts the ordering of the strongest peaks.

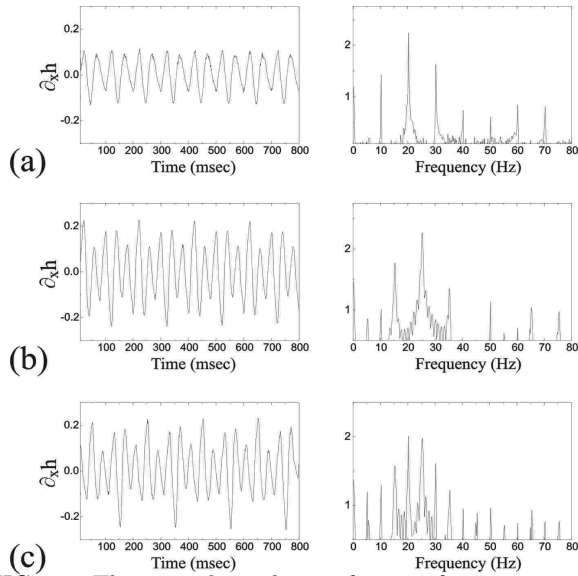


FIG. 28. The time dependence of a two-frequency experiment with even/odd driving was studied using the reflection of a laser by the surface waves. The temporal response is subharmonic (harmonic) with respect to $\omega_0 = 10$ Hz for $\chi < \chi_c$ ($\chi > \chi_c$). Time series (left) and power spectra (right) for three different regimes: (a) Typical temporal response for hexagonal pattern found for $\chi < \chi_c$. Although the $4\omega_0/2 = 20$ Hz component is the strongest, an $\omega_0 = 10$ Hz harmonic component with all of its higher harmonics is present. (b) Typical time dependence for square patterns (found for $\chi > \chi_c$). The strongest response is for $4\omega_0/2 = 25$ Hz as expected. A weaker response at the basic subharmonic $\omega_0/2 = 5$ Hz is observed together with stronger responses at other harmonics. The ordering of the harmonics agrees qualitatively with [11]. (c) Typical temporal response of a square 2MS state at χ_c . The power spectrum shows a strong response at both ω_1 (20 Hz) and ω_2 (25 Hz). All other harmonics are present with a different power distribution than in (a) and (b). System parameters here are: $50/40 Hz$, $\nu = 23$ cS, $h = 0.155$ cm, $\phi = 0^\circ$ and $\chi = 40^\circ$ (a), $\chi = 60^\circ$ (b) and $\chi_c = 53.5^\circ$ (c).

In Figure 28(c) the temporal response of the 2MS state is presented. This state has a temporal response that includes both the frequencies of the harmonic mode (a) for $\chi < \chi_c$ and those of the subharmonic one (b) for $\chi > \chi_c$. Although the power spectrum shows that both main peaks at $\omega_1/2$ and $\omega_2/2$ are of the same strength, their relative strengths can vary with the location of the laser probe.

We have seen that the 2MS state contains the two

linearly excited eigenmodes both in space and in time. Does each mode keep its distinct space-time behavior, or is there a complete mixing of the spatial and temporal components? To clarify this question, we write down a simple model for the surface height of a square 2MS state. For simplicity, we will assume a square 2MS state where both k_1 and k_2 are collinear with the same spatial phase:

$$h(r, t) = F_1(t)(\cos(k_1x) + \cos(k_1y)) + F_2(t)(\cos(k_2x) + \cos(k_2y)) \quad (7)$$

$$\frac{\partial h}{\partial x} = k_1 F_1(t) \cos(k_1x) + k_2 F_2(t) \cos(k_2x)$$

$$\frac{\partial h}{\partial y} = k_1 F_1(t) \cos(k_1y) + k_2 F_2(t) \cos(k_2y)$$

where $F_1(t) \sim \cos(\omega_1 t/2) + \dots$ and $F_2(t) \sim \cos(\omega_2 t/2) + \dots$. It is easily seen that if one selects a point $(x, y) = (\pi/2k_2, \pi/2k_1)$ then each of the components of the partial derivative $\partial h/\partial x$, $\partial h/\partial y$ has a temporal dependence of $F_1(t)$ and $F_2(t)$ respectively. Both $F_1(t)$ and $F_2(t)$ include time dependent terms retaining the parity of the linear modes: odd multiples of $(p + 1/2)\omega_0$ for a subharmonic response and even multiples of $p\omega_0$ for harmonic response.

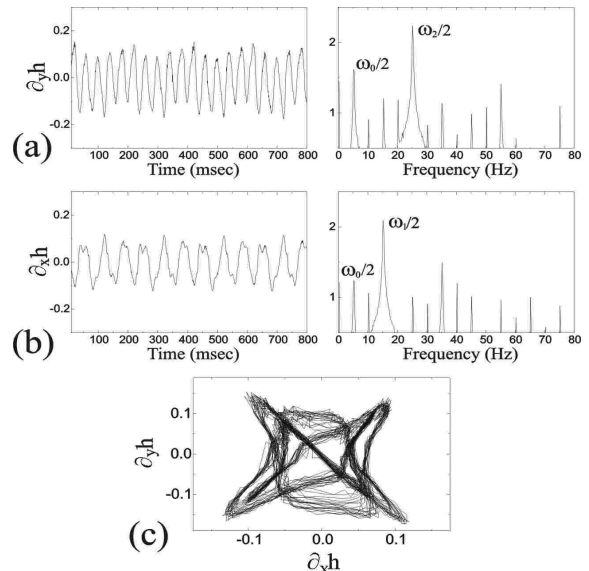


FIG. 29. The time dependence of a square 2MS state measured via the reflection of a laser at the fluid surface. Time series (left) of surface gradients, $\partial_y h$ (a) and $\partial_x h$ (b) are shown with their power spectra (right). (c) $\partial_y h$ as a function of $\partial_x h$. The separation of the temporal response (a,b) was obtained by choosing x and y along the symmetry directions. $\partial_x h$ is dominated by a $3\omega_0/2 = 15$ Hz response whereas $\partial_y h$ undergoes a $5\omega_0/2 = 25$ Hz response. System parameters used were $50/30$ Hz, $\nu = 23$ cS, $h = 0.155$ cm, $\phi = 0^\circ$ and $\chi_c = 56.3^\circ$.

As suggested by Eq. 7, experiments (see Figure 29) confirm the separation of the time dependence of the

two modes within the 2MS state. The $\partial_x h$ component has a strong $\omega_1/2$ response whereas the $\partial_y h$ component's strongest peak is at $\omega_2/2$. This strong separation of spatial time dependencies can only be observed for a few points in the (x,y) plan and, in general, the two frequencies are mixed.

C. The “unlocked” state and transition regions

Let us now consider the “unlocked” state that appears in the near vicinity of χ_c . In Figure 30 we present a typical time series of the “unlocked” state and its corresponding spatial spectra. The spatial behavior of the state varies rapidly, over time scales of order $(2\pi/\omega_0)$. In contrast to the SSS and 2MS states, in the “unlocked” state no orientational order is apparent.

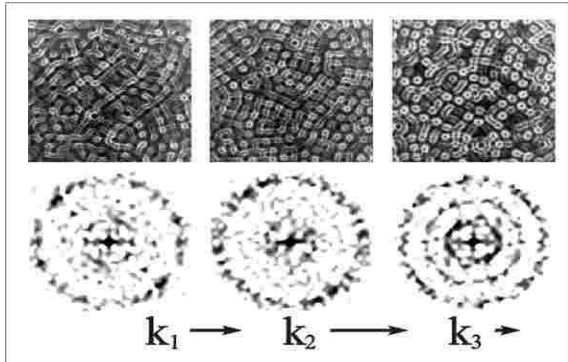


FIG. 30. In the “unlocked” state no orientational order is apparent. As in 2MS states, k_1 , k_2 and k_3 exist simultaneously but “unlocked” state spectra are diffuse and show little angular correlation. (top) Typical views of an unlocked state with corresponding spatial spectra (bottom) observed for 40/60 Hz driving at different times and fixed driving parameters. The different values of k appear with different magnitudes and orientations in each phase. Their lengths are indicated by the arrows.

Both k_1 and k_2 exist simultaneously in their spatial spectra but spatial mode locking does not occur as in the 2MS states. This is evident in their power spectra, where, generally, entire circles of radii k_1 and k_2 appear. As Figure 30d indicates, additional peaks of wavenumber k_3 corresponding to $\omega_3 = \omega_2 - \omega_1$ are sometimes observed. The “unlocked state” is a well-defined state that exists in a relatively wide region of phase space. This can be seen by defining (as in [2,15]) the following “orientational correlation function”, $C_k(\theta)$ for each value of k :

$$C_k(\theta) \equiv \Sigma_\alpha [f_k(\alpha) \cdot f_k(\alpha + \theta)] / \Sigma_\alpha [f_k(\alpha) \cdot f_k(\alpha)] \quad (8)$$

where $f_k(\alpha)$ is the Fourier transform of the wavenumber k at the polar angle α . The correlation amplitude, $Q_k = 1/2[\max C_k(\theta) - \min C_k(\theta)]$, varies between 0 and 1 for, respectively, minimal and maximal orientational order.

As Figure 31 shows, both the 2MS and hexagonal states have clear orientational order while very little residual order is apparent in the unlocked state.

As is apparent from Figure 31, the orientational amplitude drops sharply as the boundary between the 2MS and “unlocked” phases is crossed. This is demonstrated in Figure 32a–d which corresponds to the range of 5.1–5.25g in Figure 31. Between the pure hexagonal state and the “unlocked” state the hexagonal 2MS state exists. This state displays strong k_1 dominant hexagonal symmetry at most temporal phases but at other temporal phases some of the power is in the k_2 mode. Since Q_k is an average of equally time separated temporal phases the hexagonal 2MS state has a Q_k which is slightly smaller than that of the pure hexagonal state.

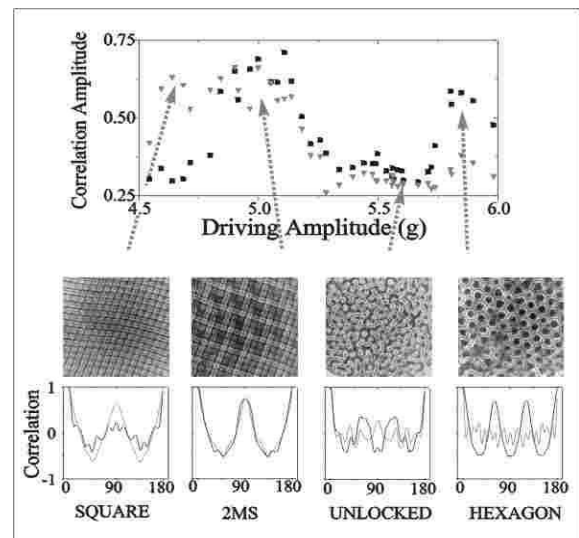


FIG. 31. Within the “unlocked” states, the correlation amplitude, Q_k drops significantly and the angular correlation function, $C_k(\theta)$, indicates only a small amount of residual order. (upper) Q_{k_1} (triangles) and Q_{k_2} (squares), averaged over a single period along the line $\chi = 58^\circ$ for 40/60 Hz driving as a function of the driving amplitude, A . This line traverses the square, square–2MS, “unlocked”, and hexagonal–2MS phases. Typical patterns in each phase are displayed (center). The symmetry of the different phases is highlighted by $C_k(\theta)$ for k_1 (grey line) and k_2 (black line) computed for typical states (θ is in degrees). The power (log scale) of k_2 relative to k_1 in each $C_k(\theta)$ is 8.3 (square), 1.1 (2MS), 0.9 (“unlocked”) and 0.2 (hexagon).

The parameter, Q_k , does not completely characterize the different transitions, since spatial FFT power spectra cannot differentiate between global and local ordering. A closer look at real–space images of the transitions presented in Figure 31 that correspond to square–2MS, “unlocked” and Hexagonal–2MS are shown respectively in Figure 32 and Figure 33. Both transitions involve an advancing front that separates two well–defined domains. The clear separation between unlocked and 2MS domains

provides further evidence that the unlocked state is indeed a distinct nonlinear state and not, simply, a transition region.

The transitions between unlocked states and the 2MS states with different symmetries differ in two ways. The sensitivity to any change of the driving parameters is much higher for the unlocked to 2MS–Hexagon transition. Whereas the transition between square 2MS and “unlocked” states occurs for a relative change of amplitude of $< 5\%$, the transition between hexagonal 2MS and hexagons can occur via a change smaller than 0.25% . The time scales of the induced transitions are also different. The first transition takes place in a nearly quasi-static reversible way, whereas the second transition (as shown in Figure 33) can occur over typical time scales of 50–1000 oscillation periods with a hysteresis of less than 0.1% . This rather sharp transition is, perhaps, due to the effects of the quadratic interactions inherent in the harmonic states. The precise duration of this transition depends on the initial and final driving parameters. As is typical of front propagation processes, the deeper one is within the hexagonal regime the faster the transition time [50].

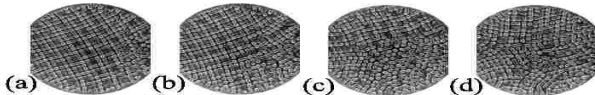


FIG. 32. The transition between the square 2MS state and the “unlocked” state occurs through a gradual process in which both states co-exist in different domains. At the transition, increasing the amplitude for constant χ constant results in (a) the global 2MS state is first disturbed by small defects at the cell’s rim. (b,c) The disturbance spreads to the cell’s center until, finally, the entire pattern is in “unlocked” state(d). This process can also occur in the reverse direction.

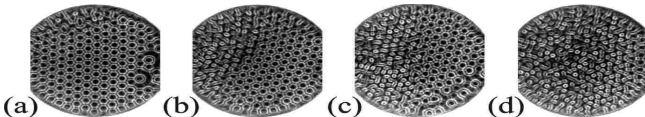


FIG. 33. A time sequence of the transition from the regular hexagonal state (a) to Hexagonal 2MS states is shown. The k_2 (60 Hz) component propagates via a front (b,c) until it dominates the entire plate and co-exists with the large length scale (d). The driving parameters are constant for this sequence.

VII. RHOMBOIDAL STATES ($2kR$) AND QUASI-PATTERNS

In the previous section we studied the three wave resonance mechanism that can form 2MS states from the interaction: $\vec{k}_3 = \vec{k}_2 - \vec{k}_1$ and $\omega_3 = \omega_2 - \omega_1$. Is the only

resonant mechanisms found in the vicinity of χ_c ?

In this section we will describe the spontaneous formation of nonlinear rhomboidal patterns, formed as a result of solely *spatially* resonant 3-wave coupling between wavevectors with distinctly different wavenumbers. This state has only previously been observed in a nonlinear optical system where the orientations of the interacting wavevectors [51] were externally imposed. Rhomboidal patterns have also been recently observed in parametrically driven ferrofluids [45]. The rhomboidal patterns described below spontaneously couple the two circles of linearly degenerate wavenumbers. These states qualitatively differ from 2MS states in that they are composed solely of the linearly excited wavevectors, k_1 and k_2 , in contrast to the additional slaved mode (k_3) necessary for 2MS formation.

The rhomboidal states observed in this system result from the non-linear interaction of k_1 and k_2 , which are waves with significantly different wavelengths. Such states have been observed numerically in a Swift–Hohenberg type models [25,27] as discussed in section I. They have also been anticipated in anisotropic models where two degenerate wavevectors are resonant with an externally imposed wavenumber [52], in nonlinear optical systems [53,54], and in the analysis of the Faraday instability excited with two frequencies [33,30]. Both rhomboidal states and superlattice patterns have also been recently predicted to occur as a result of two bistable modes coupling to a zero-mode [55].

The rhomboidal states observed in this system differ distinctly from rhomboids resulting from slightly “distorted” hexagonal states [56,57]. “Distorted hexagons”, predicted to be stable in models with derivative-coupled quadratic terms, may arise due to either initial or boundary conditions [58]. These states have been observed in reaction-diffusion systems [57], convection in an imposed shear flow [59], and flux line lattices in superconductors [60].

A. Experimental conditions

We have observed rhomboid states using both Dow-Corning 200 oils with kinematic viscosities, ν , of 8.7, 23, 47, 87 cS (at 30°C) and TKO-77 vacuum pump fluid with $\nu = 184$ cS (at 33°C) in fluid layers whose depth varied between $0.1 < h < 0.55$ cm. The 2 wavenumber rhombic ($2kR$) states described in this section were all generated with $m/n = 2/3$ and $12 < \omega_0/2\pi < 45$ Hz or $m/n = 4/5$ with $10 < \omega_0/2\pi < 20$ Hz. Frequency combinations of 25/50, 30/60, 40/80, 40/56, 45/63, 48/68, 50/70, 55/75, 55/77, 30/50, 40/70, 45/60, 50/65, 50/80, 52/68, 60/84, 60/100 did *not* generate $2kR$ states.

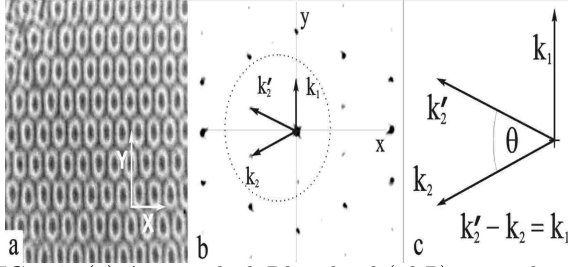


FIG. 34. (a) A typical $2kR$ Rhomboid ($2kR$) state observed for $2/3$ driving and $\omega_0/(2\pi) = 25$ Hz, $\nu = 23$ cS, and $h = 0.2$ cm. The axis y is defined by the direction of k_1 . (b) The power spectrum (c) illustrates the simple resonance condition $\vec{k}'_2 - \vec{k}_2 = \vec{k}_1$ that generates these states. \vec{k}'_2 and \vec{k}_2 correspond to $\omega_2 = 3\omega_0/2$ while \vec{k}_1 corresponds to $\omega_1 = 2\omega_0/2$. θ here is 41° .

In Figure 34 we present a typical image of a $2kR$ pattern. Although k_1 and k_2 are the linearly unstable wavenumbers [14] excited by ω_1 and ω_2 , their orientation is determined by the 3-wave non-linear interaction that yields the resonant triad: $\vec{k}'_2 - \vec{k}_2 = \vec{k}_1$, where $|\vec{k}'_2| = |\vec{k}_2| = k_2$. The higher harmonics in the figure may either be real or could occur as an artifact of the imaging. An additive three-wave resonance occurs for $1/2$ forcing where the resonance $\vec{k}'_1 + \vec{k}_1 = \vec{k}_2$ governs the selected pattern. In this case, the resulting pattern (see section VIII) is a superposition of hexagonal lattices composed of the two scales.

The observation of $2kR$ states solely for driving ratios $2/3$, $4/5$ and $1/2$ is entirely consistent with Silber and Skeldon's [30] predictions (see ID 2) that 3-wave interactions coupling the wavenumbers k_1 and k_2 are only allowed when two odd-parity waves are coupled to a wave with even parity. Thus, $\vec{k}'_1 + \vec{k}_1 = \vec{k}_2$ coupling is allowed for odd/even frequency ratios such as $1/2$, and $\vec{k}'_2 - \vec{k}_2 = \vec{k}_1$ coupling occurs in even/odd forcing, such as $2/3$ and $4/5$. It is interesting that we have not observed these states for other frequency ratios. It is possible that 2MS states are preferred for all but the simplest frequency ratios since, for higher ratios, linearly stable tongues corresponding to wavenumbers close to the value of k_3 (defined by $\omega_3 = \omega_2 - \omega_1$) are more dense.

A typical phase space in which $2kR$ states are observed is presented in Figure 4 (right). For values of χ that are far from χ_c , the phase diagram is similar those described in sections III and VI. The $2kR$ state exists in the near vicinity of χ_c , and replaces both the 2MS and unlocked states. This region is bounded for $\chi > \chi_c$ by squares and for $\chi < \chi_c$ by k_1 -dominant DHS states that are mixed with oscillons [20] (see [19]). At higher values of ν and h (e.g. $\nu = 47$ cS, $h = 0.3$ cm, $\nu = 87$ cS, $h = 0.5$ cm) square and hexagonal patterns only exist near onset. Upon increase of A both types of patterns become rolls. The $2kR$ state is, however, unaffected by the state preceding it. They appear for a similar range of ϕ . The

transition to DHS and oscillon states also occurs as in Figure 4.

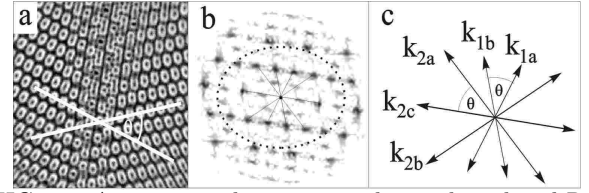


FIG. 35. A common phenomenon observed in the $2kR$ region of phase space is the formation of two domains of $2kR$ states (left) which are oriented with a relative angle of θ that is also the angle between the two larger vectors \vec{k}_2, \vec{k}'_2 forming the $2kR$ state. A similar phenomenon can also be observed in domains formed by triblock copolymers [61].

$2kR$ states are not always correlated throughout the entire system. At relatively low values of A , $2kR$ states can sometimes be found in 2 or 3 domains, as shown in Figure 35. The angle separating two such domains is identical to the angle θ between \vec{k}_2 and \vec{k}'_2 , as defined in Figure 34(b). This type of domain separation is also observed in “knitting patterns” [61], formed by triblock copolymers near a bistable point. (These new materials have a reciprocal lattice structure similar to $2kR$ states).

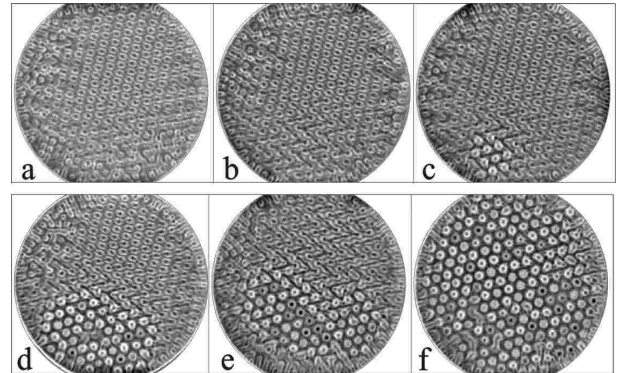


FIG. 36. The transition from the $2kR$ state to the DHS state occurs through an “explosive” process in which a spatial domain of hexagons forms and rapidly increases in size. Six images (a-f) of this process taken at 1.5 second intervals for an experiment performed with $66/44$ Hz driving for $\nu = 23$ cS, and $h = 0.2$ cm at mixing angle $\chi = 70^\circ$. Note areas of mixed $2kR$ and hexagonal domains around the perimeter of the hexagonal area (clearly seen in upper half of (e)). In this process the driving parameters are *fixed*.

Let us return to the description of the typical phase space. As increasing the driving amplitude A strengthens the nonlinear interactions between the waves, $2kR$ domains coalesce at higher levels of excitation. Further increase of A yields a hysteretic bifurcation to the “Double Hexagonal Superlattice” state (DHS), where oscillons are formed at the maxima of the pattern (see [19]). In Figure 36 we present a time sequence of the transition from a global $2kR$ state to a DHS state by means of rapid front

propagation. Only at the final stages of this process does the pattern bifurcate into the high-amplitude state consisting of oscillons superimposed on a DHS background (see Sec. V and [19]). The opposite transition from the DHS to the $2kR$ state has a qualitatively different character. Small k_2 -dominated wavelength domains penetrate the DHS from the perimeter of the cell in a way similar to the transition from hexagons to SSS. The transition is not reversible and can have a small hysteresis (under 1%).

Both 2MS and $2kR$ states are observed for the driving ratios $2/3$ and $4/5$. In [22] the dimensionless parameter $\delta/h \equiv (\nu/\omega_{ave})^{1/2}/h$ (where $\omega_{ave} \equiv (\omega_2 - \omega_1)/2$) was shown to govern the selection between the two patterns. For $\phi = 0$, 2MS/“Unlocked” states exist above $\delta/h \sim 0.12 - 0.17$, while $2kR$ states exist below. This critical range of δ/h was obtained for a broad range of both h ($0.1 \leq h \leq 0.6\text{cm}$) and ν ($8.7 \leq \nu \leq 186\text{cS}$). The parameter δ/h is the ratio of two important physical scales of the system: the ratio of the viscous boundary layer length, where the flow is rotational, to the fluid layer’s height. This parameter, in essence, defines the region of applicability of the Zhang and Vinals, quasipotential approximation. $(\delta/h)^2$ is the ratio of the dissipative time to the driving time scales. In Lioubashevski et al. this number was critical for determining pattern selection by single frequency excitations [39,36]. Thus, this transition suggests that high dissipation in the system favors the 2MS over the $2kR$ states. This may result from the (linear) broadening of unstable tongues [35] that occurs when dissipation in the system is increased. This broadening would make the linearly stable wavenumber observed in 2MS states, k_3 , more accessible.

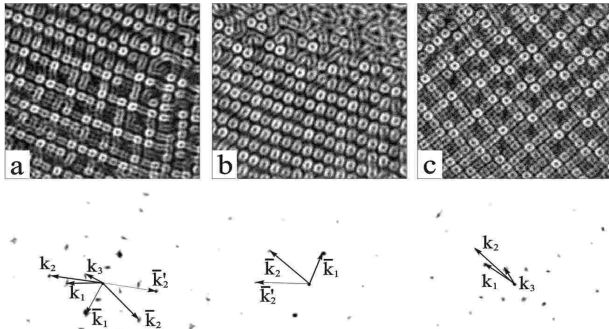


FIG. 37. When δ/h is at the transition between $2kR$ and 2MS stability zones (b) $2kR$ and (c) 2MS exist in the same vicinity. ($A = 6.59g$, $\chi = 60.6^\circ$ for $2kR$ and $A = 6.53g$, $\chi = 61.4^\circ$ for 2MS). (a) A transient state combining the two resonances was obtained for the parameters of (b). Parameters here were $2:3$ driving, $\omega_0 = 25$ Hz, and $\delta/h = 0.12$.

In the transition regime of δ/h , both 2MS and $2kR$ states can coexist, as shown in Figure 37 for $\delta/h = 0.12$.

In this region, at fixed values of δ/h , small changes in either A or χ can result in globally stable states of either type. As shown in Figure 37a, transient states in which both states are present can also result in this regime. In these states both resonant mechanisms can operate *concurrently* in different spatial regions of the fluid cell.

As the two driving frequencies are commensurate, the phase variable, ϕ in Eq. 1 is a relevant control parameter. As was shown in the experimental work of Muller and Edwards and Fauve (see Sec. IC) changing ϕ can affect pattern selection. Typically, the $2kR$ state exists over the range $-20^\circ < \phi < +15^\circ$. The phase space presented in Figure 4 (right) is typical for $0.16 < h < 0.22$ cm and $\nu = 23$ cS. In Figure 38 we show how changing the angle ϕ causes the pattern to change from the $2kR$ to the 2MS state. The transition is not abrupt and in some regions localized patches of both states can co-exist. In general, the size of the region in phase space where a single $2kR$ domain exists decreases with the distance from $\phi = 0^\circ$. Because $\phi = 180^\circ$ is equivalent, for $2/3$ driving, to $\phi = 0^\circ$, the $2kR$ is also stable at this angle. The strong effect of changes in ϕ is consistent with the predictions of Zhang et al. (see Sec. ID 1) who showed how ϕ can affect the mode coupling function $\beta(\theta)$. Silber et al. [33] have recently demonstrated that changing ϕ affects the $2kR$ resonance by varying the non-linear coefficients of the model equations describing the system.

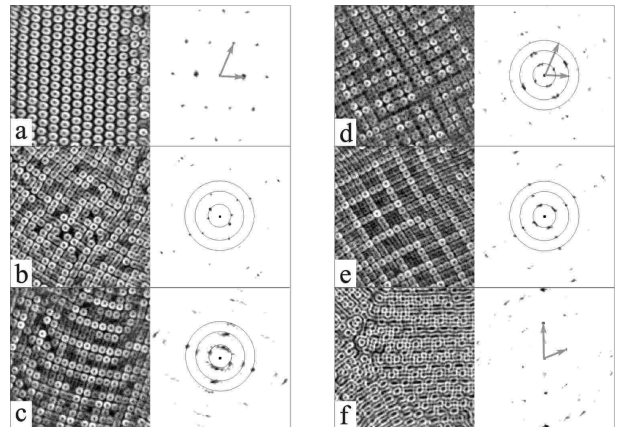


FIG. 38. The effect of changing ϕ in the driving can be seen in the sequence of images (left) and their power spectra (right) for different values of ϕ . While for $\phi = 0^\circ$ (a) a $2kR$ state is stable and global, increasing ϕ from (b) 20° and (c) 30° transforms the system to a stable 2MS state at (d) 90° . Increasing the angle to (e) 120° , (f) 150° reverses the process and finally for $\phi = 180^\circ$ a global $2kR$ re-emerges. The 3 concentric circles indicate the magnitude of the three 2MS wavevectors (k_1, k_2, k_3), while the gray arrows indicate the wave vectors of the $2kR$ state \vec{k}_1, \vec{k}_2 . These measurements were performed for $2/3$ driving with system parameters: $\omega_0/(2\pi) = 25$ Hz, $\nu = 23$ cS, and $h = 0.2$ cm at mixing angle $\chi = 70.5^\circ$

B. Temporal behavior

The temporal behavior of the $2kR$ state is similar to that of the even/odd 2MS states, where the time dependence in different directions is qualitatively different. Like the even/odd 2MS states, different directions can have dominant subharmonic or harmonic components. In Figure 39 we see how the harmonic nature of the $2kR$ is manifested. A time translation of π/ω_0 shifts the observed pattern by a spatial translation of $\pi/|\vec{k}_2 + \vec{k}'_2|$ in the x direction (as defined in Figure 34a). The overall spatio-temporal behavior of the $2kR$ state is consistent with Eq. (9).

$$h(t, x, y) = [a_1 \cos(\omega_0 t) + a_2 \cos(2\omega_0 t) + \dots] \cos(\vec{k}_1 \cdot \vec{x}) \\ + [b_1 \cos(\omega_0 t/2) + b_2 \cos(3\omega_0 t/2) + \dots] \times (9) \\ [\cos(\vec{k}_2 \cdot \vec{y}) + \cos(\vec{k}'_2 \cdot \vec{y})].$$

The fact that the two directions, $\vec{x} \parallel \vec{k}_1$ and $\vec{y} \perp x$ (as defined in Figure 34) each exhibit *different* time dependence is demonstrated in Figure 40. This typical time series of the x and y components of the surface gradient of this state at a single point is similar to that presented in Figure 29 for the 2MS state. By our choice of axes, the $\partial_x h$ component contains mainly the $\omega_1/2, 2\omega_1/2 \dots$ peaks, while the dominant frequencies in the y direction are $(\omega_2 - \omega_1)/2, \omega_2/2 \dots$. Arbitrary \vec{x} and \vec{y} directions will contain both k_1 or k_2 eigenmodes. This orientational dependence may prove to be a general characteristic of superlattice states. When a *single* mode is dominant, the predictions of Zhang and Vinals [11] are in good quantitative agreement with our measurements of the relative peak intensities. In the vicinity of χ_c , when 2 modes are concurrently excited, this analysis does not apply and a new theoretical framework is needed.

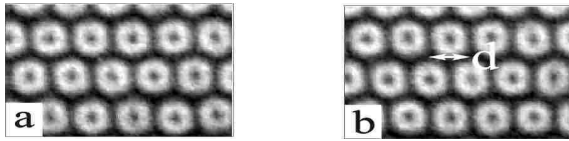


FIG. 39. A typical $2kR$ state taken for $\omega_0/(2\pi) = 25$ Hz, $\nu = 23$ cS and $h = 0.2$ cm, in temporal phases separated by half of the common excitation time $T/2 = \pi/\omega_0$. The time translation is equivalent to a spatial translation of magnitude $d = \pi/(|\vec{k}_2 + \vec{k}'_2|)$. This feature can be reproduced by Eq. 9.

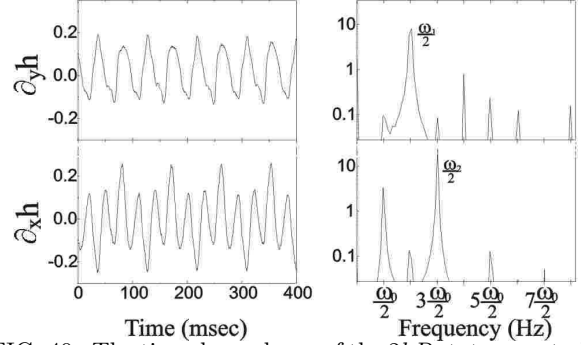


FIG. 40. The time dependence of the $2kR$ state was studied using the reflection of a laser by a point on the fluid surface. The directional derivatives $\partial_x h$ and $\partial_y h$ as a function of time (left) and their corresponding power spectra (right) show that each direction has a different temporal dependence. (The x, y directions are defined in Figure 34a). $\partial_y h$ is dominated by the k_2 and k'_2 components with dominant frequency $\omega_2/2$ and $\partial_x h$ corresponds to the k_1 component with dominant frequency $\omega_1/2$. This figure was taken from [22]. The parameters for the above were $\omega_0/(2\pi) = 22$ Hz, $\nu = 23$ cS, $\phi = 0^\circ$ and $h = 0.2$ cm

In low viscosity fluids ($\nu = 8.7$ cS, $0.1 < h < 0.2$ cm, and $\delta/h < 0.13$) an interesting variant of the pure $2kR$ state is observed whose symmetry changes with its temporal phase (see [22]). At different temporal phases pure hexagonal, mixed hexagonal and $2kR$ phases can be seen. Interestingly, this state exists for a significantly broader range of ϕ ($-70^\circ < \phi < 70^\circ$) than the pure $2kR$ state. Together with the vector triad characteristic of $2kR$ states, coupling with the difference vector, $\vec{k}_2 - \vec{k}_1$, is also observed in the spatial spectra of these states.

C. Tuning of the resonant angles and quasi-pattern formation

The angle θ between the two wavevectors \vec{k}_2 and \vec{k}'_2 , can be tuned by changing the different system parameters. Since the values of k_1 and k_2 are roughly determined by the dispersion relation $\omega(k)$, the angle θ can be varied by changing ω_0, ν , or h while leaving m/n constant. This is demonstrated in Figure 41. The value of θ can be calculated for a specific mixing angle χ using the numerical method developed by Kumar and Tuckerman [13].

D. Three frequency driving

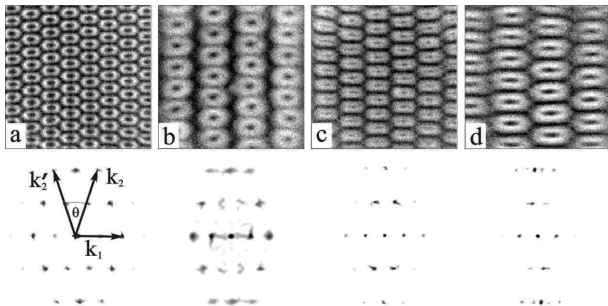


FIG. 41. The resonant angle between k_1' and k_2 varies with the parameters of the experiment. We obtain angles of (a) 36° for system parameters of $\omega_0/(2\pi) = 25$ Hz, $\nu = 47$ cS, and $h = 0.25$ cm, (b) 33° for system parameters of $\omega_0/(2\pi) = 15$ Hz, $\nu = 87$ cS, and $h = 0.5$ cm, (c) 32° for system parameters of $\omega_0/(2\pi) = 25$ Hz, $\nu = 87$ cS, and $h = 0.5$ cm and (d) 29° for system parameters of $\omega_0/(2\pi) = 20$ Hz, $\nu = 184$ cS, and $h = 0.54$ cm. All images were taken from a 9×9 cm² square in the center of the circular plate.

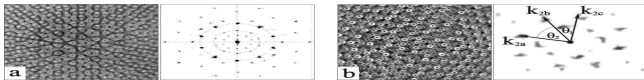


FIG. 42. (a) A 10-fold quasiperiodic pattern and its power spectrum is observed for $\omega_0/(2\pi) = 30$ Hz, $\nu = 47$ cS and $h = 0.33$ cm. Circles are drawn with radii k_1 (inner) and k_2 (outer). For these parameters $\theta = 360^\circ/10$ and five $2kR$ regions combine to form the quasipattern. For $\omega_0/(2\pi) = 30$ Hz, $\nu = 23$ cS and $h = 0.2$ cm (b) an nearly 8-fold symmetric pattern is seen. This pattern, however, is actually a deformed quasipattern since the $2kR$ value here of $\theta = 41^\circ$ does not evenly divide 360° . Instead of a single angle, two different angles $\theta_1 = 41^\circ$ and $\theta_2 = 49^\circ$ are observed in the power spectrum.

As suggested by [25,26], when rhomboidal states exist the tuning of θ can provide a well-defined mechanism in which quasipatterns of any desired symmetry may be formed. When $360/\theta = p$, an integer number of adjacent triads can be formed. As conjugate pairs of triads are always formed, the integer p must always be even (as observed in [16,27]). This is demonstrated in Figure 42 where the formation of perfect 10-fold quasicrystalline patterns and approximate 8-fold quasi-patterns occurs for values of θ that are tuned to these resonant ($360/\theta = n$) angles. As the power spectra of these states indicate, each of the inner circle of peaks of magnitude k_1 is coupled by a triad resonance with two peaks of magnitude k_2 along the outer circle. When $\theta \approx 41^\circ$, a symmetric quasi-pattern is not possible and a distorted 8-fold quasi-pattern, as shown in Figure 42b, occurs.

Having observed the distorted 8-fold quasipatterns described in Figure 42b, we attempted to stabilize these “*asymmetric*” quasi-patterns by modifying the driving. Muller in [12] added a third frequency perturbation to break the spatial phase symmetry in the subharmonic regime and thereby control the transition between triangles and hexagons. This motivated us to add a third frequency in order to enable the excited wavevectors k_1 and k_2 to spatially lock to the value of $\theta = 45^\circ$ for which 8-fold quasi-patterns can naturally form. We used the following driving function:

$$A[a_1 \cos(p_1 \omega_0 t) + a_2 \cos(p_2 \omega_0 t + \phi_1) + a_3 \cos(p_3 \omega_0 t + \phi_2)] \quad (10)$$

where the total driving amplitude is given by A and the normalized amplitude ratios by $a_1 : a_2 : a_3$ with $a_1 + a_2 + a_3 = 1$. $p_1 : p_2 : p_3$ are the three frequency ratios $p_1 < p_2 < p_3$ and ϕ_1, ϕ_2 are the phase differences with respect to the p_1 components.

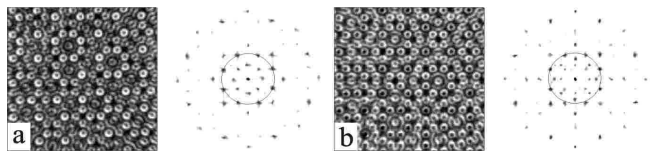


FIG. 43. Two temporal phases of an 8-fold quasi-pattern observed for three-frequency driving (a,b). This state is temporally subharmonic and was observed in the region where the distorted 8-fold quasi-patterns were observed (see Figure 42). This state was observed in a 50/75/100 Hz experiment with driving amplitude ratio $a_1 : a_2 : a_3$ equal to 0.16 : 0.36 : 0.48 and a phase difference of 180° between the 100 Hz component and the two other components.

Using 2:3:4 driving we indeed observed a perfect 8-fold quasi-pattern. In Figure 43 we show images and power spectra of this state at two temporal phases. This state is subharmonic in time and can be observed in the region where 10-fold quasi-patterns and 8-fold distorted quasi-patterns were observed for the 2/3 experiments described above. Interestingly, this state was exceedingly stable and existed within a single domain over a wide range of parameters (note the sharp peaks in Figure 43). This is in sharp contrast to the distorted 8-fold state shown in Figure 42 which existed in both a narrow range of parameters and, as evident in its diffuse spectrum, had a tendency to break up into domains. It is possible that the third frequency allows the $2kR$ mechanism to form the quasi-pattern through the relaxation of the ratio between k_1 and k_2 and thereby the angle between them. This state was observed in a 50/75/100 Hz experiment with ratios of driving amplitudes $a_1 : a_2 : a_3$ equal to 0.16 : 0.36 : 0.48, where the single-frequency critical accelerations for these frequencies are, respectively, 2.56g,

4.40g and 6.91g (yielding ratios of a 0.18 : 0.32 : 0.49) and phase differences $\phi_1 = 0^\circ$, $\phi_1 = 180^\circ$. Although the third frequency acceleration is not small here, it is still below the critical value for single-frequency excitation at 100Hz and wavevectors corresponding to the 100 Hz component were not observed.

E. Transition states to rhomboids

Figure 44 shows an expanded view of the $2kR$ phase space around χ_c (see Figure 4 (right)). The region shown, lies in the subharmonic region of phase space ($\chi > \chi_c$) where square patterns form at threshold. For χ close to χ_c the transition region and the $2kR$ region is relatively narrow compared to the transition region for larger values of χ .

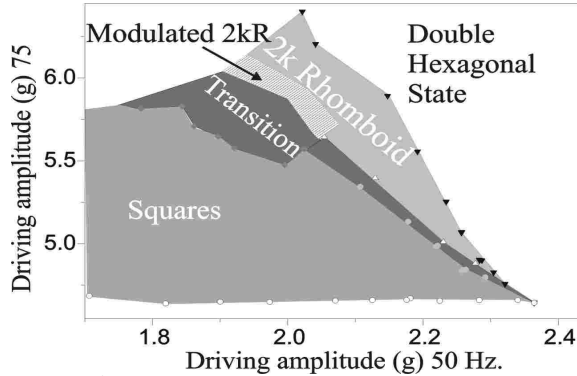


FIG. 44. An expanded view of the phase space described in Figure 4 (right). Transition states between square and $2kR$ states are formed by a superposition of a square state with one (two) sets of $2kR$ triad vectors. Between the $2kR$ and transition states, a modulated $2kR$ state exists in which an additional \vec{k}_2 component parallel to the \vec{k}_1 component exists.

The transition from the square symmetry region to the $2kR$ state is perhaps more interesting than the transition between squares to square 2MS discussed in (subsection VIC). While the square-2MS transition occurs through the formation of an “additional” set of wavevectors (of different wavenumber) that combine with each of the primary wavevectors that initially formed the squares, the square- $2kR$ transition has a qualitatively different nature. Here, the basic square symmetry is not only broken, but is actually *replaced* by a pattern of completely different symmetry. In $2kR$ states, one of the two k_2 wavevectors that are initially perpendicular to each other in the square state is replaced by a k_2 wavevector whose orientation forms the angle θ that is determined by the magnitude of the k_1 wavevector which defines the $2kR$ rhomboidal pattern.

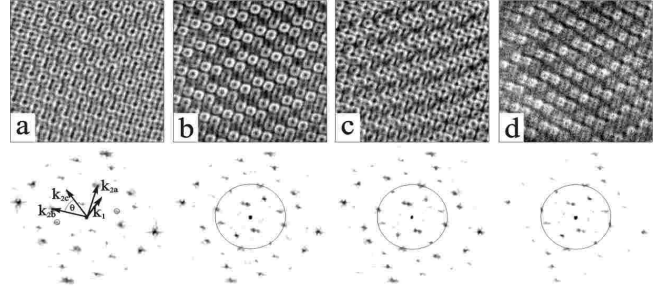


FIG. 45. A typical time sequence of the transition state is shown with the corresponding power spectra (bottom). The wavevectors (\vec{k}_{2a} , \vec{k}_{2b}) generating the squares appear together with a third wavevector, \vec{k}_{2c} that is oriented at an angle of $\theta = 41^\circ$ to \vec{k}_{2b} . The above experiment was made for system parameters of $\omega_0/(2\pi) = 27Hz$, $\nu = 23cS$, $\phi = 0^\circ$, $\chi = 69^\circ$ and $h = 0.2cm$.

A typical “transition” state at different temporal phases is shown in Figure 45. The transition occurs through the formation of one or two additional wavevectors of magnitude k_2 , (\vec{k}_{2c} in Figure 45a). These new wavevectors are aligned at the $2kR$ resonant angle θ with respect to the k_2 wavevectors (\vec{k}_{2a} and \vec{k}_{2b}) which form the squares. Although additional k_2 vectors could, in theory, form $2kR$ triads with *all* of the original k_2 wavevectors, empirically, we find that only one of the initial k_2 directions is selected. This is possibly due to the fact that the self-interaction of the *harmonic* k_1 wavevectors prefers a hexagonal (rather than a square) arrangement.

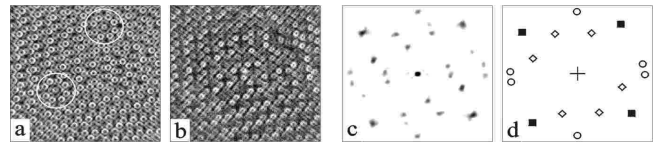


FIG. 46. The transition states between square and $2kR$ symmetry do not usually form a global state. (a) and (b) show different phases of a typical transition state that is formed by three domains. In (a) white circles note areas where two $2kR$ domains intersect. The power spectrum of (a) is shown in (c) and the wavevectors are noted in (d) by (squares) the primary square wavevectors, (circles) $2kR$ -resonant k_2 wavevectors, and (diamonds) the k_1 wavevectors. Since the power spectra reflect the entire pattern, three separate sets of $2kR$ triads can be observed in the same spectrum. The system parameters here are $\omega_0/(2\pi) = 30Hz$, $\nu = 23cS$, $h = 0.2cm$, $\chi = 71.4^\circ$ and $\phi = 0^\circ$.

Thus the transition pattern that is formed is a superposition of a k_2 *square* state with a $2kR$ state. All other wavevectors seen are formed by secondary interactions of these wavevectors. Generally, the transition state breaks the symmetry of the square pattern in a single direction. Since the transition state is usually not global, two domains can form and at their common border one can observe structures that retain the four-fold symmetry, as

indicated by the white circles in Figure 46a.

In the near vicinity of χ_c , the transition patterns appear as in Figure 45, and their rhomboidal character is apparent. Farther away from χ_c , the appearance of the transition state is more similar to squares, as the orthogonal k_2 wavevectors are more dominant.

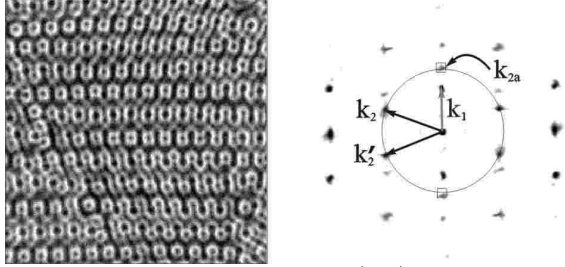


FIG. 47. “Modulated $2kR$ ” states (left) are variants of the $2kR$ states formed when (see the power spectrum (right)) an additional wavevector of magnitude k_2 , \vec{k}_{2b} , parallel to \vec{k}_1 is generated. The system parameters are $\omega_0/(2\pi) = 22$ Hz, $\nu = 23$ cS, $\phi = 0^\circ$ and $h = 0.2$ cm.

For $\chi > 70^\circ$ we observe a variant of the $2kR$ state, shown in Figure 47, which forms between the “transition” and the $2kR$ regions (see Figure 44). This state, which we call a “modulated” $2kR$, consists of a modulation of the regular $2kR$ triad by an additional wavevector of the magnitude and temporal behavior of the larger frequency component. This state is formed by the superposition of a $2kR$ state with an additional wave vector of magnitude k_2 that is oriented parallel to the k_1 wave vector (see Figure 47 (right)). This wavevector retains the time dependence of the k_2 mode and generates a spatial and temporal modulation, similar to that induced in the SSS mode, in the \vec{k}_1 direction (x in Figure 34a). A possible mechanism that can generate a “modulated” $2kR$ state is a 2MS resonance between the two collinear wavevectors \vec{k}_1 and \vec{k}_2 that produces a \vec{k}_3 wavevector along the same direction. This is verified by comparison with the square 2MS pattern obtained for the same parameters with $\phi = 90^\circ$ (see Figure 38e). This mechanism is supported by our observations of the “modulated” $2kR$ states for only relatively low values of ω_0 for which the wavevectors \vec{k}_1 , \vec{k}_2 and \vec{k}_3 , forming the 2MS state, are nearly parallel.

VIII. ADDITIONAL RESONANT STATES

A. States observed for odd/odd parity driving

The work of Silber et al. [33] indicates that the possible three-wave resonant interactions between excited and damped modes depend on the parity of the driving. For odd/odd driving no 3-wave resonant interactions between k_1 and k_2 are expected since both modes

are temporally subharmonic (see Sec. ID1). When considering four wave interactions, however, these restrictions are no longer valid. Below, we describe two experiments conducted with odd/odd driving that indeed show that 4-wave resonant interactions can be found both in the vicinity of χ_c , where one mode is strongly excited and the other only weakly damped, and far from χ_c where the interactions involve an excited mode and a single strongly damped mode corresponding to the subharmonic frequency, $\omega_0/2$.

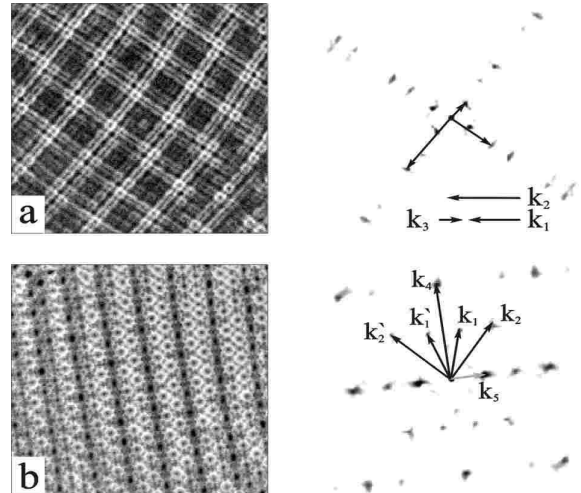


FIG. 48. A 5/7 ratio yields both the 2MS resonance (a) and a four-wave resonance (b). In the 2MS power spectrum (a right) the three vectors are nearly parallel obeying the resonance $\vec{k}_3 = \vec{k}_2 - \vec{k}_1$. In (b right) the power spectrum reveals a qualitatively different resonance: $\vec{k}_1 + \vec{k}_1' = \vec{k}_2 + \vec{k}_2' \equiv \vec{k}_5$. This resonance produces additional vectors such as \vec{k}_5 that are sums and differences of the original wavevectors involved. The experimental parameters are 55/77 Hz driving frequencies, $\nu = 23$ cS, and $h = 0.2$ cm. In (a) $\phi = 90^\circ$, $\chi = 72.8^\circ$ and in (b) $\phi = 0^\circ$, $\chi = 70.8^\circ$.

For $\chi > \chi_c$ a 5/7 frequency ratio can produce a square 2MS state in the vicinity χ_c . This, however, is not the only resonantly locked pattern that can be observed at this driving ratio. Mixing angles typically 3–5 degrees beyond χ_c results in the formation of the state shown in Figure 48b. The spatial spectrum of this state indicates that it is formed by a qualitatively different mechanism. The original square pattern, formed by two orthogonal k_2 wavevectors, is broken by an additional pair of k_1 wavevectors, whose orientation is determined by the four-wave resonance condition: $\vec{k}_1 + \vec{k}_1' = \vec{k}_2 + \vec{k}_2'$. This resonance produces additional vectors that are sums and differences of the original wavevectors involved. States similar to these have been previously observed in vertically oscillating convection experiments [62], where 3-wave interactions are forbidden.

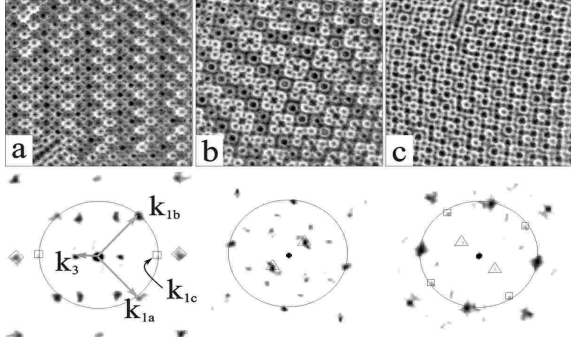


FIG. 49. In an experiment with 3/5 (60/100 Hz) driving, patterns with square symmetry (or slightly rhombic) dominate for mixing angles $\chi < \chi_c$. The primary wavenumber is of magnitude k_1 (circles in a,b,c). When the driving is increased, the primary symmetry is broken by a small wavevector of magnitude k_3 (enclosed in triangles). These states are observed for parameters $\nu = 23$ cS, and $h = 0.2$ cm both at mixing angle close to χ_c (a) $\chi = 69.6^\circ$ and far from χ_c (b) $\chi = 48.1^\circ$ and (c) $\chi = 58.7^\circ$. A possible mechanism for the large scale symmetry breaking is a resonant four-wave interaction. The power spectrum (a bottom) reveals the existence of additional vectors of magnitude k_1 (enclosed by squares). The interaction of \vec{k}_{1c} with the sum of the original vectors $\vec{k}_{1a} + \vec{k}_{1b}$ (enclosed by diamonds) results in a new vector $\vec{k}_3 = \vec{k}_{1c} - (\vec{k}_{1a} + \vec{k}_{1b})$ whose scale is consistent with $k(\omega_0/2)$.

In odd/odd driving both sides of phase space exhibit subharmonic temporal response. Unlike the 5/7 driving that produces hexagons for $\chi < \chi_c$ (despite the subharmonic temporal response), experiments performed using 3/5 driving with $\omega_0 = 20$ Hz yield square symmetric patterns for $\chi > \chi_c$ and nearly square patterns (rhomboids with an angle of 84°) for $\chi < \chi_c$. Here, a state exhibiting a different mode of 4-wave coupling far from χ_c is presented in Figure 49. Like the SSS states, these patterns result from a symmetry breaking bifurcation for $\chi_c + 20^\circ > \chi > \chi_c$. The power spectrum reveals that in addition to the dominant pair of orthogonal wavevectors, (\vec{k}_{1a} and \vec{k}_{1b} in Figure 49) an additional wavevector of the same magnitude, \vec{k}_{1c} , is created along the bisector of \vec{k}_{1a} and \vec{k}_{1b} . The vector sum of these three wavevectors of magnitude k_1 produces a smaller wavevector of magnitude $k_3 = k_{1c} - (k_{1a} + k_{1b})$. The scale of \vec{k}_3 is consistent with $k(\omega_0/2)$, as determined by the linear dispersion relation. Thus, as in the case of 2MS states, a symmetry-breaking slaved mode, \vec{k}_3 is excited by a nonlinear resonance.

B. States satisfying more than one resonance condition

We have observed a number of cases where states which satisfy more than a single resonance condition were se-

lected by the system. These states are generally stable in a relatively wide range of phase space. Here we present a number of examples of such multiply-resonant nonlinear states.

We have seen that SSS-I states result from a primary hexagonal symmetry broken by a wavevector of size $k_c/2$. A similar mechanism can occur for square or rhomboid patterns. In Figure 50 we show a *spatially* subharmonic state, obtained using 5/8 driving, where a rhomboid, is formed by two wavevectors of magnitude k_1 (\vec{k}_1 and \vec{k}'_1 in Figure 50) via the additive $2kR$ resonance: $\vec{k}_1 + \vec{k}'_1 = \vec{k}_2$. The spatial period of the rhomboid is doubled by the appearance of two *new* wavevectors of size $k_1/2$, ($\vec{k}_1/2$ and $\vec{k}'_1/2$ in Figure 50). This state was observed for a mixing angle $\chi = \chi_c - 1^\circ$. An additional spatial resonance is apparent. The vectors, $\vec{k}_1 - \vec{k}'_1 + \vec{k}_1/2$ and $\vec{k}_1 - \vec{k}'_1 - \vec{k}_1/2$ both form vectors of length k_2 (see k_{2a} and k_{2b} in Figure 50). This “extra” 4-wave resonance may be the result of spatial mode-locking. It may be possible that this extra resonance causes the selection and resultant stability of this state.

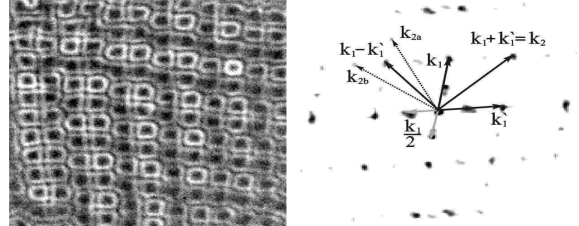


FIG. 50. An image (left) and power spectrum (right) of a *spatially* subharmonic state where a rhomboid is formed by $\vec{k}_1 + \vec{k}'_1 = \vec{k}_2$ where k_1 (k_2) are generated by the $5\omega_0$ ($8\omega_0$) frequencies. The pure rhomboid symmetry is broken by two spatially subharmonic vectors, $\vec{k}_1/2$ and $\vec{k}'_1/2$. The vectors k_{2a} and k_{2b} are formed by additional resonances: $\vec{k}_{2a} = \vec{k}_1 - \vec{k}'_1 + \vec{k}_1/2$ and $\vec{k}_{2b} = \vec{k}_1 - \vec{k}'_1 - \vec{k}_1/2$. This state appears for 50/80 Hz driving for $\nu = 23$ cS and $h = 0.2$ cm for $\chi \sim \chi_c - 1^\circ$.

Another example of a state satisfying two resonance conditions is presented in Figure 51. This state, which is only observed in 1/2 driving experiments, is both a hexagonal 2MS state as well as an SSS-II state. The driving ratio of 1/2 is unique since ω_3 (given by $\omega_3 = \omega_2 - \omega_1$) is equal to ω_1 . Thus, the wavenumber k_3 , excited by ω_3 , coincides with the wavenumber k_1 , excited by ω_1 . Therefore [11], a resonant triad is formed involving only the two critical wavenumbers k_1 and k_2 . In this case SSS-II and 2MS states coincide for $20 \text{ Hz} < \omega_0 < 50 \text{ Hz}$. The resonance that is formed is identical to the SSS-II resonance found for odd/even driving in the harmonic region (see Sec. IV B), where the wavevectors of magnitude q and K of the SSS-II state are replaced by wavevectors of respective magnitude k_1 and k_2 . The resonance condition for the 1/2 experiment can be written as $\vec{k}_1 + \vec{k}'_1 = \vec{k}_2$.

The SSS-II type resonance is possible since, for the system parameters used, the ratio k_2/k_1 is close to $\sqrt{3}$. The same resonance was also observed by Wagner et al. for a two mode subharmonic-harmonic interaction in a single-frequency, lubrication-limit experiment [42]. In their experiment, for special values of h and ω , two modes with temporal responses of $\omega/2$ and ω and with spatial wavenumbers k_1 and k_2 , are excited by single-frequency forcing.

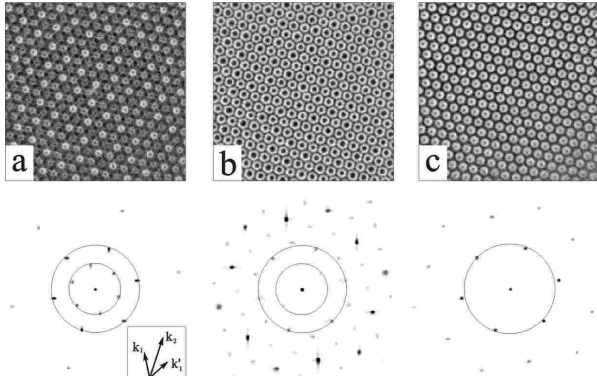


FIG. 51. Images (a-c top) and the corresponding power spectra (a-c bottom) of different temporal phases of a SSS-II (2MS) state observed for 1/2 driving in the harmonic region of phase space at system parameters of $\nu = 23$ cS, 40/80 Hz and $h = 0.155$ cm. The pattern was observed in the vicinity of χ_c for $\chi > \chi_c$. This state resembles SSS-II states observed for 2/3 driving although here a typical super-hexagon cell is $\pi/3$ symmetric whereas the SSS-II state generally has $\pi/6$ rotational symmetry.

In our last example, we present an example of a state where multiple resonance conditions are simultaneously satisfied. When this occurs, we find that the stability of a pattern is significantly enhanced. This state contains features of most of the states described above. This single state includes a 2MS resonance, a DHS resonance (with a $1/\sqrt{7}$ sublattice), an SSS-II type resonance and an “additive” and “subtractive” $2kR$ resonance. This state was observed for 2/3 driving ($\omega_0 = 20$ Hz) with $\phi = 117^\circ$ and is shown in Figure 52.

As can be seen in the power spectrum (Figure 52 right) a double lattice with wavenumber k_2 at an angle of 22.2° produces the familiar DHS structure described in Section III. However, in this case the smallest inner hexagon has a magnitude of k_3 , which is associated with $\omega_3 = \omega_2 - \omega_1$ frequency, while the second inner hexagonal set of wavevectors has a magnitude of k_1 . This resonance is very stable and exists in a single domain. This stability is perhaps due its multiply-resonant nature. In Figure 53 a time sequence is shown of the different phases of this state is presented.



FIG. 52. A state formed by simultaneous multiple resonances obtained with 2/3 driving with the same parameters used to form a $2kR$ state at $\phi = 0$, $\omega_0/(2\pi) = 20$ Hz, $\nu = 23$ cS, $\chi = 59^\circ$, and $h = 0.2$ cm, but with a phase of $\phi = 117^\circ$. The wavevectors of magnitude k_3 are formed both from the resonance $k_2 - k_2' = k_3''$ as well as the resonance $k_2 - k_1 = k_3$. In addition, the condition satisfying the DHS structure is satisfied and the hexagonal sublattice formed by the k_3 wavevectors spans the entire lattice. k_1 , k_2 , and k_3 are, respectively, noted by squares, circles, and diamond symbols.

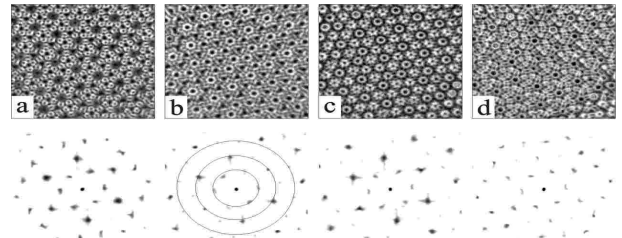


FIG. 53. Different temporal phases of the state described in Figure 52 taken for constant values of the driving parameters. Circles of radii k_1 (middle circle), k_2 (outer circle) and k_3 (inner circle) are drawn in (b). At different temporal phases, different scales appear dominant.

IX. CONCLUSIONS

The work described in this paper provides, for the first time, a partial, but coherent, experimental picture of both the nonlinear states generated by two-frequency forcing as well as their domains of existence in phase space and the nonlinear interactions that generate them. As demonstrated above, the space of nonlinear patterns formed by two interacting unstable modes is very rich. Our understanding of the types of structures and their selection is just beginning. Predicted nonlinear three-wave resonances [30], however, appear to govern nonlinear pattern selection only for the *simplest* ratios (2/3 and 1/2). Recent theoretical advances made by Silber et al. in the analysis of two-frequency Faraday system in the vicinity of the co-dimension 2 point [30,33] suggest that at least some of the features discovered by our experiments can be reproduced by amplitude equations derived using the quasi-potential approximation (e.g. [11]). In addition, recent work [23,40,41] indicates that many of the superlattice states found far from χ_c may be qualitatively understood as representations of invariant subgroups of broken hexagonal symmetry. A quantitative theory that describes the important regime of two or more concu-

rently unstable modes for arbitrary height and viscosity has still to be developed.

Some of the major results of this work are summarized below:

- The temporal symmetry of the driving determines which resonant interactions *can* occur between the primary excited modes. A number of distinct three and four wave interactions between excited modes and between slaved and excited modes were experimentally observed.
- Factors such as the dimensionless dissipation in the system and the driving phase ϕ can play an important role in the nonlinear interaction mechanism selected by the system. ϕ is a convenient parameter for comparison with theory, as, in contrast to the system's dissipation, its value does not play a role in the validity of the theoretical (e.g. [11]) approximation used.
- Symmetry-breaking can often occur via modes that nonlinearly couple to the original set of modes. The symmetry-breaking modes tend to be arranged in invariant subgroups of the original symmetry group.
- In many cases, slaved modes can be non-linearly excited by the parametrically amplified linear modes. The availability of slaved modes (determined by the ratio of the driving frequencies) is important in the selection of the final nonlinear states. This provides a nontrivial selection mechanism for nonlinear states.
- A theoretically predicted mechanism [25,26] for producing quasi-patterns was for the first time experimentally observed. By tuning the system parameters to satisfy a resonance condition $2n$ -fold quasi patterns can be produced for any desired n .

We believe that both the states and nonlinear mechanisms described in this work should be of general importance to a wide class of parametrically-driven nonlinear systems. Such systems include parametrically-driven fluid systems, non-linear optical systems [63,64,51,65,44], nonlinear wave interactions in superfluid helium [66,67], magnetically-driven ferrofluids [45], and possibly nonlinearly coupled mechanical systems. Although the behavior of systems driven by 2-frequency forcing is, itself, important. Understanding the spatio-temporal behavior of such systems is but a first step in understanding the general behavior in space and time of nonlinear systems driven by multiple frequencies. The work presented here is an important building block on the road to understanding these more complex systems.

We gratefully acknowledge the support of the Israel Academy of Sciences (Grant no. 203/99).

-
- [1] S. Douady, Journal of Fluid Mechanics **221**, 383 (1990).
 - [2] D. Binks and W. van de Water, Physical Review Letters **78**, 4043 (1997).
 - [3] A. Kudrolli and J. P. Gollub, Physica D **97**, 133 (1996).
 - [4] K. Kumar and K. M. S. Bajaj, Physical Review E **52**, R4606 (1995).
 - [5] E. Bosch and W. van de Water, Physical Review Letters **70**, 3420 (1993).
 - [6] S. Ciliberto, S. Douady, and S. Fauve, Europhysics Letters **15**, 23 (1991).
 - [7] A. B. Ezerskii, M. I. Rabinovich, V. P. Reutov, and I. M. Starobinets, Soviet Physics JETP **64**, 1228 (1986).
 - [8] B. J. Gluckman, P. Marq, J. Bridger, and J. P. Gollub, Physical Review Letters **71**, 2034 (1993).
 - [9] A. Kudrolli and J. P. Gollub, Physical Review E **54**, R1052 (1996).
 - [10] L. Daudet, V. Ego, S. Manneville, and J. Bechhoefer, Europhysics Letters **32**, 313 (1995).
 - [11] W. Zhang and J. Vinals, Journal of Fluid Mechanics **341**, 225 (1997).
 - [12] H. W. Muller, Physical Review Letters **71**, 3287 (1993).
 - [13] T. Besson, W. S. Edwards, and L. S. Tuckerman, Physical Review E **54**, 507 (1996).
 - [14] K. Kumar, Proceedings of the Royal Society of London, Series A (Mathematical, Physical and Engineering Sciences) **452**, 1113 (1996).
 - [15] H. Arbell and J. Fineberg, Physical Review Letters **81**, 4384 (1998).
 - [16] W. S. Edwards and S. Fauve, Comptes Rendus de l'Academie des Sciences, Serie II (Mecanique, Physique, Chimie Sciences de la Terre et de l'Univers) **315**, 417 (1992).
 - [17] W. S. Edwards and S. Fauve, Physical Review E **47**, R788 (1993).
 - [18] W. S. Edwards and S. Fauve, Journal of Fluid Mechanics **278**, 123 (1994).
 - [19] H. Arbell and J. Fineberg, Physical Review Letters **85**, 756 (2000).
 - [20] P. B. Umbanhowar, F. Melo, and H. L. Swinney, Nature **382**, 793 (1996).
 - [21] A. Kudrolli, B. Pier, and J. P. Gollub, Physica D **123**, 99 (1998).
 - [22] H. Arbell and J. Fineberg, Physical Review Letters **84**, 654 (2000).
 - [23] M. Silber and M. R. E. Proctor, Physical Review Letters **81**, 2450 (1998).
 - [24] D. Binks, M. T. Westra, and W. van de Water, Physical Review Letters **79**, 5010 (1997).
 - [25] H. W. Muller, Physical Review E **49**, 1273 (1994).
 - [26] T. Frisch and G. Sonnino, Physical Review E **51**, 1169 (1995).
 - [27] R. Lifshitz and D. M. Petrich, Physical Review Letters **79**, 1261 (1997).
 - [28] A. C. Newell and Y. Pomeau, Journal of Physics A (Mathematical and General) **26**, L429 (1993).
 - [29] W. Zhang and J. Vinals, Journal of Fluid Mechanics **336**,

- 301 (1997).
- [30] M. Silber and A. C. Skeldon, *Physical Review E* **59**, 5446 (1999).
- [31] J. D. Crawford, *Reviews of Modern Physics* **63**, 991 (1991).
- [32] J. D. Crawford, *Physica D* **52**, 429 (1991).
- [33] M. Silber, C. M. Topaz, and A. C. Skeldon, *Physica D* **143**, 205 (2000).
- [34] D. P. Tse, A. M. Rucklidge, R. B. Hoyle, and M. Silber, *Physica D* **146**, 367 (2000).
- [35] K. Kumar and L. S. Tuckerman, *Journal of Fluid Mechanics* **279**, 49 (1994).
- [36] O. Lioubashevski, J. Fineberg, and L. S. Tuckerman, *Physical Review E* **55**, R3832 (1997).
- [37] F. Simonelli and J. P. Gollub, *Journal of Fluid Mechanics* **199**, 471 (1989).
- [38] O. Lioubashevski *et al.*, *Physical Review Letters* **83**, 3190 (1999).
- [39] O. Lioubashevski, H. Arbell, and J. Fineberg, *Physical Review Letters* **76**, 3959 (1996).
- [40] D. P. Tse, A. M. Rucklidge, R. B. Hoyle, and M. Silber, *Physica D* **146**, 367 (2000).
- [41] S. M. Rucklidge, A. M. and F. J., to appear .
- [42] C. Wagner, H. W. Muller, and K. Knorr, *Physical Review E* **62**, R33 (2000).
- [43] C. Wagner, H. W. Muller, and K. Knorr, *Physical Review Letters* **83**, 308 (1999).
- [44] A. Logvin Y., T. Ackemann, and W. Lange, *Physical Review A (Atomic, Molecular, and Optical Physics)* **55**, 4538 (1997).
- [45] H. J. Pi, S. Y. Park, J. Lee, and K. J. Lee, *Physical Review Letters* **84**, 5316 (2000).
- [46] T. Ackemann, A. Logvin Yu, A. Heuer, and W. Lange, *Physical Review Letters* **75**, 3450 (1995).
- [47] R. Herrero *et al.*, *Physical Review Letters* **82**, 4627 (1999).
- [48] J. L. Hammack and D. M. Henderson, *Annual Review of Fluid Mechanics* **25**, 55 (1993).
- [49] E. Pampaloni, S. Residori, S. Soria, and F. T. Arecchi, *Physical Review Letters* **78**, 1042 (1997).
- [50] J. Fineberg and V. Steinberg, *Physical Review Letters* **58**, 1332 (1987).
- [51] A. V. Mamaev and M. Saffman, *Physical Review Letters* **80**, 3499 (1998).
- [52] W. Zimmermann *et al.*, *Europhysics Letters* **24**, 217 (1993).
- [53] A. J. Scroggie and W. J. Firth, *Physical Review a* **53**, 2752 (1996).
- [54] M. Hoyuelos, P. Colet, M. S. Miguel, and D. Walgraef, *Physical Review E* **58**, 2992 (1998).
- [55] M. Bachir, S. Metens, P. Borckmans, and G. Dewel, *Europhys. Lett.* **54**, 612 (2001).
- [56] E. A. Kuznetsov, A. A. Nepomnyashchy, and L. M. Pismen, *Physics Letters A* **205**, 261 (1995).
- [57] G. H. Gunaratne, Q. Ouyong, and H. L. Swinney, *Physical Review E* **50**, 2802 (1994).
- [58] P. C. Matthews, *Physica D* **116**, 81 (1998).
- [59] P. Hall and R. E. Kelly, *Physical Review E* **52**, 3687 (1995).
- [60] M. Yethiraj, D. M. Paul, C. V. Tomy, and E. M. Forgan, *Physical Review Letters* **78**, 4849 (1997).
- [61] U. Breiner, U. Krappe, E. L. Thomas, and R. Stadler, *Macromolecules* **31**, 135 (1998).
- [62] J. L. Rogers, M. F. Schatz, O. Brausch, and W. Pesch, *Physical Review Letters* **85**, 4281 (2000).
- [63] M. Tlidi, P. Mandel, and M. Haelterman, *Physical Review E* **56**, 6524 (1997).
- [64] R. Martin, A. J. Scroggie, G. L. Oppo, and W. J. Firth, *Physical Review Letters* **77**, 4007 (1996).
- [65] D. Leduc, M. LeBerre, E. Ressayre, and A. Tailet, *Physical Review a* **53**, 1072 (1996).
- [66] D. Rinberg, V. Cherepanov, and V. Steinberg, *Physical Review Letters* **76**, 2105 (1996).
- [67] D. Rinberg, V. Cherepanov, and V. Steinberg, *Physical Review Letters* **78**, 4383 (1997).